AN INVESTIGATION OF THE MECHANICAL PROPERTIES OF INCONEL ALLOY 740H, POLYCRYSTALLINE GRAPHENE AND TETRA-GRAPHENE

by

Elnaz Haddadi

A dissertation submitted to the faculty of
The University of North Carolina at Charlotte
in partial fulfillment of the requirements
for the degree of Doctor of Philosophy in
Mechanical Engineering

Charlotte

2024

Approved by:

Dr. Alireza Tabarraei

Prof. Ronald E. Smelser

Prof. Harish Cherukuri

Dr. Vincent (Tobi) Ogunro

ABSTRACT

ELNAZ HADDADI. An Investigation of the Mechanical Properties of Inconel Alloy 740H, Polycrystalline Graphene and Tetra-graphene. (Under the direction of DR. ALIREZA TABARRAEI)

This PhD dissertation focuses on three distinct areas of study: Inconel Alloy 740H, polycrystalline graphene, and tetragraphene (TG). These materials each have their unique characteristics and applications, and this dissertation seeks to study and reveal their mechanical properties.

The first project of this dissertation concentrates on the development and validation of a Chaboche constitutive model, incorporating combined nonlinear isotropic and kinematic hardening rules, to accurately predict the stress-strain behavior of Inconel Alloy 740H. Additionally, the material behavior of Inconel 740H is also predicted by only using the kinematic hardening rule to understand the difference in results. Inconel 740H is a high-temperature, nickel-based superalloy known for its exceptional mechanical strength, creep resistance, and corrosion resistance, making it highly suitable for extreme environmental applications. The research focuses on determining the material parameters of the unified Chaboche constitutive model and validating its accuracy using experimental data obtained from uniaxial strain-controlled loading tests. The experimental data covers a wide temperature range from the room temperature up to 600°C, with strain ranges spanning from 0.375% to 0.5%. The results, derived from both methods, demonstrate the model's effectiveness in capturing the complex mechanical behavior of Inconel Alloy 740H under varying conditions, providing a valuable tool for design and engineering applications in high-temperature environments.

The second project explores the mechanical properties of polycrystalline graphene, bridging the nanoscale to macroscale through a multiscale molecular dynamics (MD) finite element (FE) modeling approach. At the nanoscale, MD simulations are em-

ployed to study crack propagation and mechanical behavior. To address the limitations of atomic level simulations for large scale polycrystalline systems, FE analysis is used. To this aim, a multiscale modeling approach is adopted, initiating MD simulations on bicrystalline graphene sheets with different grain boundaries (GB) and atomic structures under uniaxial tension loading. These simulations provide insights into the local elastic properties of grain boundaries (GBs) using the cohesive zone model. Subsequently, the local properties derived using MD simulations are incorporated into FE simulations, which enables the modeling of large scale polycrystalline graphene sheets considering the effect of the grain boundaries. The grains are modeled as pristine graphene, and the simulations are repeated with varying grain sizes to investigate their impact on mechanical properties such as Young's modulus and fracture stress. The results reveal a significant relationship between the grain size and the mechanical properties of polycrystalline graphene, indicating a crucial role of the grain size in its behavior.

The final project of this dissertation investigates the mechanical properties of tetragraphene (TG), a quasi-2D semiconductor carbon allotrope composed of hexagonal and tetragonal rings, to address the limitations of graphene in electronic applications. MD simulations are employed to understand the fracture properties of triple-layered TG sheets with distinct atomic structures under mixed mode I and II loading. The effect of loading phase angle, temperature, crack edge chirality, and crack tip configuration on the crack propagation path and critical stress intensity factors are investigated. The findings indicate that the critical stress intensity factor and crack propagation path are influenced by these parameters, and their effect is discussed in detail.

DEDICATION

This work is dedicated first to my parents, who provided the much-needed motivation to keep me focused on the finish line. Secondly, to my brother, who always cheered me on and stood by me through everything.

This would not have been possible without the continual support and love they provided throughout my life.

Thank you all

ACKNOWLEDGEMENTS

Over the past years in the mechanical engineering and engineering science department, I have had the great privilege of studying and learning under my advisor, Dr. Alireza Tabarraei. He has provided significant guidance and support as my Ph.D. supervisor throughout these years. His knowledge of material science, and fracture mechanics, and his practical experiences were conducive to my research. In the pandemic situation caused by COVID-19, Dr. Tabarraei was constantly and patiently leading me to proceed with my research.

I would also like to thank my committee members, Dr. Ronald Smelser, Dr. Harish Cherukuri, and Dr. Vincent (Tobi) Ogunro, for their support throughout this process.

TABLE OF CONTENTS

LIST OF TABLES

LIST OF FIGURES

CHAPTER 1: Introduction

The main goal of materials science is to understand, design, and develop materials with specific properties and characteristics to meet various practical needs and applications. The primary goals within this field include understanding material behavior, tailoring properties, safety and reliability, and technological advancement. In this dissertation, 3 projects have been investigated. The first project (Inconel 740 Material Modeling) aims to gain a deep understanding of the material behavior of Inconel 740 through material modeling. The second project (Fracture Analysis of Polycrystalline Graphene) focuses on understanding the impact of grain size and grain boundaries on the mechanical properties of polycrystalline graphene. This project involves modeling the behavior of polycrystalline graphene at different scales. Lastly, the third project (Fracture Properties of Tetragraphene) discovers the fracture properties of tetragraphene through computational methods, particularly molecular dynamics simulations.

1.1 Inconel 740 Material Modeling

Inconel 740, a nickel-based superalloy renowned for its exceptional mechanical and corrosion resistance, has gained significant importance in various industries such as aerospace, gas turbines, nuclear reactors, and petrochemicals. Its unique properties make it an ideal candidate for applications in high-temperature and high-stress environments where components face rigorous operating conditions. The development of a reliable material model for Inconel 740 is of great importance to fully comprehend its behavior under diverse operating conditions. This model serves as a powerful tool for engineers and researchers to accurately predict the alloy's response to thermal and

mechanical loads, enabling the design of safe and efficient components. Moreover, understanding the material's behavior is fundamental in optimizing its performance and ensuring the structural integrity of critical components. With an increasing demand for high-performance materials in extreme environments, the establishment of a comprehensive material model for Inconel 740 contributes significantly to advancements in engineering and technology. This project aims to address the need for such a material model and presents its development and validation, thereby offering valuable insights into the behavior of Inconel 740 under various stress and temperature regimes.

Different techniques have been used in the past to model material behavior [1, 2, 3]. In this project, the Chaboche model is utilized to develop the material model for Inconel 740. This unified model has obtained considerable attention due to its capability to simulate cyclic plasticity, creep relaxation, and hardening. The Chaboche model has been successfully implemented into numerous commercial finite element software packages, enhancing its practical applicability and further solidifying its place as a go-to constitutive model for materials exhibiting cyclic plasticity and creep behavior. Extensive work by Chaboche [4, 5] and others [6, 7, 8, 9] have contributed to the model's popularity and refinement. Various research efforts have explored the application of the Chaboche model to study cyclic plasticity, creep relaxation, ratcheting, and multiaxial thermomechanical fatigue in a diverse range of materials [10, 11, 12]. These studies have demonstrated the model's effectiveness in accurately predicting material behavior under cyclic loading and high-temperature conditions. Chaboche, who is credited with the unified model, has published extensively on the topic [4, 5]. Additionally, Kang [13] has also provided reviews about kinematic hardening models. Several investigations on the ratcheting phenomenon have been conducted implementing the Chaboche model, such as the work by Bari [6]. Additionally, the work by XU and Yue [7] utilized a single backstress Chaboche model, excluding isotropic hardening, to demonstrate the ratcheting phenomenon. To mitigate errors in the

model, additional backstress terms were added. For instance, the work by Bari and Hassan [6] incorporates the use of a triple backstress Chaboche model for parameter determination. Similar work was completed by Koo [14], who investigated the ability of a dual backstress Chaboche model in a ratcheting simulation. Several researchers have utilized the Chaboche model to investigate cyclic inelastic behavior and multiaxial thermomechanical fatigue (TMF) problems of various materials. Tong [10] employed the uniaxial Chaboche model to study the cyclic behavior of a nickel-based alloy, while Barrett [11] modified the model for investigating multiaxial TMF problems. In addition, Koo and Kwon [12], Zhang [8], and Bernhart [15] also applied the multiaxial Chaboche model to simulate the cyclic plasticity of martensitic steels and study the isotropic hardening strain memory effect. Additionally, several investigations have been performed to assess the accuracy of analytical models by comparing them with experimental results and numerical simulations for determining mechanical parameters [9].

Various numerical methods have also been utilized to predict the mechanical response of materials in numerous research studies. Prior research has emphasized estimating material parameters from experimental data and optimizing the results to develop an accurate constitutive model. In this study, a dual backstress Chaboche constitutive model is developed using an experimental database acquired under various conditions to determine the material properties of Inconel Alloy 740H. To achieve this, an experimental database provided by EPRI, which includes uniaxial strain-controlled loading tests at varying temperatures, ranging from room temperature up to 600°C, and strain ranges spanning from 0.375% to 0.5% is used. These tests can capture the material's response under representative operating conditions. The material model's parameters are then determined through a process, optimizing the model to closely match the experimental data. This step ensures that the model accurately represents the material's actual behavior across the entire range of tem-

peratures and loading conditions. The validation of the developed material model is performed by comparing the model's predictions with experimental data. The validation tests include diverse loading conditions, including strain-controlled loading at various temperatures and strain ranges. The successful correlation between the model's predictions and the experimental results serves as a validation, affirming the accuracy and reliability of the developed material model in simulating the mechanical response of Inconel Alloy 740H.

1.2 Fracture Analysis of Polycrystalline Graphene

A fundamental understanding of the mechanical behavior of the materials is of significant importance to use them safely in aerospace, automobile, electronics, nuclear power, and chemical industries. Many components in these industries are subjected to thermo-mechanical fatigue (TMF) loads and are working under high temperature and pressure conditions [16, 17, 18, 19, 20]. Therefore, the safe structural design of such components is complicated due to the several life-limiting mechanisms interacting and contributing simultaneously to the failure. Hence, understanding the material behavior under these conditions is necessary to estimate the lifetime of the components and have a safe design.

Among the materials used in the industry, graphene is considered a great candidate material for many applications [21, 22, 23, 24, 25, 26] due to its extraordinary features, therefore, studying the mechanical properties and fracture mechanism of the graphene is vital. To this end, we are investigating the fracture behavior of the polycrystalline graphene sheets and the effect of the grain size on their mechanical properties from nanoscale to macroscales.

While many companies became interested in pursuing large scale polycrystalline graphene sheets [27] in industry, there is still a lack of knowledge in multiscale modeling of polycrystalline graphene on a large scale. Modeling the behavior of the large scale polycrystalline is not possible by using molecular dynamics (MD) simulations

because of the limitations in the atomic level simulations, and it demands utilizing other methods such as finite element analysis (FEA) to model the mechanical and fracture properties of large graphene sheets.

One way to study the fracture properties is using cohesive zone models. However, extraction of the cohesive laws through experimental work is challenging. Atomistic simulations are conducted [28, 29, 30, 31, 32] to extract the cohesive laws, but in all of them, only one or two-grain boundaries are considered. To model the behavior of the polycrystalline graphene by using the cohesive laws, it is necessary to include different grain boundaries with different atomic structures.

In this study, to address this issue, we are conducting a multiscale analysis using FE and MD simulations to study the crack propagation and the mechanical behavior of the polycrystalline graphene sheet on a large scale. As mentioned, large scale polycrystalline graphene sheets have received noticeable attention in industries while there is a lack of knowledge in this area, thus, multiscale modeling of their fracture behavior is of high importance and still challenging due to the extracting cohesive laws of different grain boundaries with different atomic structure from MD simulations and utilizing them in FEA. In this research, we are studying the multiscale modeling of polycrystalline graphene on a large scale for the first time by using machine learning interatomic potentials (MLIPs) to describe the interaction between the carbon atoms. The cohesive laws are extracted from different grain boundaries, and the results are implemented in FE simulations to investigate the effect of the grain size and grain boundaries on the mechanical behavior of the large scale polycrystalline graphene sheet. These findings would have significant outcomes for the mass production of graphene materials for industrial applications.

1.3 Fracture Properties of Tetragraphene

Over the last few years, nanomaterials have attracted significant attention in the field of materials science and engineering [33, 34, 35, 36, 37, 38], providing a founda-

tion for the advancement of technologies with unmatched properties. Among these remarkable nanomaterials, tetragraphene (TG) is a two-dimensional carbon allotrope that demonstrates extraordinary characteristics and structural stability. TG is not a genuinely one-atom-thick structure due to its structural buckling and is often regarded as a "quasi-2D" structure [39]. In contrast to graphene, which is a semimetal and suffers from the lack of an intrinsic band gap [40, 41], which is limiting its direct application in electronic devices, TG possesses a unique lattice structure that offers exciting opportunities for tailoring its electronic band structure [42]. This property opens new perspectives for employing TG in electronic applications, potentially overcoming one of the major challenges faced by graphene-based devices. Moreover, the fourfold symmetry of TG introduces electronic anisotropy, signifying that its electronic properties may vary significantly with direction. This interesting characteristic can be creatively employed in designing novel electronic devices with tailored functionalities and precise electronic behavior, adding an extra layer of versatility to the material's potential applications.

While graphene's mechanical and fracture properties have been extensively studied [43, 44, 45], more investigation is needed to understand the fracture characteristics of other graphene-like two-dimensional materials such as TG. Unlike graphene's flat structure, TG's atomic structure is more intricate, with a triple-layered arrangement in each sheet. Consequently, TG's failure mechanisms are more complex than those of graphene. As a result, a distinct analysis of TG's fracture properties is essential, as they may vary significantly from those of graphene.

Given the challenges in conducting experiments at the nanoscale, computational methods such as MD and density functional theory (DFT) have become invaluable in studying the properties of two–dimensional materials. Brandao et al. [39] utilized MD simulations to evaluate the mechanical properties of TG. Their simulations indicated a transition from a crystalline to an amorphous structure induced by applying

temperature and/or tension. De Vasconcelos et al. [46] studied the stability, as well as the electronic and magnetic properties of TG nanoribbons, by using first-principles calculations based on the DFT. They examined how the electronic properties of these nanoribbons depend on their width, chirality, and edge atom reconstruction. De Vasconcelos et al. [47] analyzed the electronic properties of TG using the DFT method, and they determined that it shows metallic or semiconducting behaviors, depending on its structural parameters. Furthermore, it has been noticed that TG has high electronic mobility with smaller cohesion energy than penta-graphene. Hence, TG could be a good choice for high-performance electronic devices [48]. Wei et al. [42] explored how TG behaves under uniaxial tensile strain and found that it has superior ultrahigh strength and ductility by using DFT calculations. Kilic and Lee [49] utilized DFT calculations to examine the stability, structural, mechanical, thermal, electronic, and optical properties of TG and its hydrogenated derivatives. Based on their findings, there is a decrease in thermal conductivity and an increase in specific heat capacity in hydrogenated derivatives of TG. Moreover, they found that hydrogenation reduces in-plane stiffness and Young's modulus, but increases ultimate strength. In another study conducted by Kilic and Lee [50], the stability of TG and its fluorinated derivatives is investigated from different aspects such as energetic, dynamic, thermal, and mechanical through DFT calculations. This project aims to explore the fracture properties of TG through molecular dynamic simulations, with a specific focus on examining the crack propagation path and critical stress intensity factors under mixed mode I and II loading conditions.

1.4 Dissertation Structure and Outcomes

This dissertation focused on understanding the mechanical behavior of materials which is essential for safe design in industries like aerospace, automotive, electronics, and related industries. Chapter 2 focuses on Inconel 740, a nickel-based superalloy vital to high-stress environments. The research aims to develop a material model to

predict its behavior under thermal and mechanical loads, contributing to safer and more efficient component design. Chapter 3 centers on polycrystalline graphene, exploring its behavior at large scales using a combination of finite element analysis and molecular dynamics simulations by considering machine learning interatomic potentials (MLIPs) for interatomic interactions [51]. Extracting cohesive laws for different grain boundaries is a key objective. Finally, Chapter 4 investigates mechanical and fracture properties of tetragraphene (TG). The research explores TG's mechanical behavior and fracture properties. This study employs computational methods to understand TG's behavior under different loading conditions.

REFERENCES

[1] Alireza Tabarraei, Jeong-Hoon Song, and Haim Waisman. A two-scale strong discontinuity approach for evolution of shear bands under dynamic impact loads. *International Journal for Multiscale Computational Engineering*, 11(6), 2013.

[2] Shank S Kulkarni and Alireza Tabarraei. An ordinary state based peridynamic correspondence model for metal creep. *Engineering Fracture Mechanics*, 233:107042, 2020.

[3] G Venkatramani, S Ghosh, and M Mills. A size-dependent crystal plasticity finite-element model for creep and load shedding in polycrystalline titanium alloys. *Acta materialia*, 55(11):3971–3986, 2007.

[4] Jean-Louis Chaboche. A review of some plasticity and viscoplasticity constitutive theories. *International journal of plasticity*, 24(10):1642–1693, 2008.

[5] J-L Chaboche, Pascale Kanoute, and Farida Azzouz. Cyclic inelastic constitutive equations and their impact on the fatigue life predictions. *International journal of plasticity*, 35:44–66, 2012.

[6] Shafiqul Bari and Tasnim Hassan. Anatomy of coupled constitutive models for ratcheting simulation. *International Journal of Plasticity*, 16(3-4):381–409, 2000.

[7] BX Xu and ZF Yue. Study of ratcheting by the indentation fatigue method with a flat cylindrical indenter. part II. finite element simulation. *Journal of materials research*, 22(1):186–192, 2007.

[8] Z Zhang, Denis Delagnes, and Gérard Bernhart. Anisothermal cyclic plasticity

modelling of martensitic steels. *International Journal of Fatigue*, 24(6):635–648, 2002.

[9] Sunish Vadakkeveetil, Arash Nouri, and Saied Taheri. Comparison of analytical model for contact mechanics parameters with numerical analysis and experimental results. *Tire Science and Technology*, 48(3):168–187, 2020.

[10] Jie Tong, Z-L Zhan, and B Vermeulen. Modelling of cyclic plasticity and viscoplasticity of a nickel-based alloy using chaboche constitutive equations. *International journal of Fatigue*, 26(8):829–837, 2004.

[11] Richard A Barrett, PE O'Donoghue, and Sean B Leen. An improved unified viscoplastic constitutive model for strain-rate sensitivity in high temperature fatigue. *International Journal of Fatigue*, 48:192–204, 2013.

[12] Gyeong-Hoi Koo and Ji-Hyun Kwon. Identification of inelastic material parameters for modified 9Cr-1Mo steel applicable to the plastic and viscoplastic constitutive equations. *International Journal of Pressure Vessels and Piping*, 88(1):26–33, 2011.

[13] Guozheng Kang. Ratchetting: recent progresses in phenomenon observation, constitutive modeling and application. *International Journal of Fatigue*, 30(8):1448–1472, 2008.

[14] Sungyong Koo, Jungmoo Han, Karuppasamy Pandian Marimuthu, and Hyungyil Lee. Determination of chaboche combined hardening parameters with dual backstress for ratcheting evaluation of AISI 52100 bearing steel. *International Journal of Fatigue*, 122:152–163, 2019.

[15] Gérard Bernhart, G Moulinier, Olivier Brucelle, and Denis Delagnes. High temperature low cycle fatigue behaviour of a martensitic forging tool steel. *International Journal of fatigue*, 21(2):179–186, 1999.

[16] RJI Beatt, WL Birch, SE Hinton, M Kelly, MJ Pully, GRL Wright, and W Wright. Two-shift operation of 500 MW boiler/turbine generating units. *Proceedings of the Institution of Mechanical Engineers, Part A: Power and Process Engineering*, 197(4):247–255, 1983.

[17] Magdalena Speicher, Florian Kauffmann, Jae-Hyeok Shim, and Mahesh Chandran. Microstructure evolution in alloy 617 B after a long-term creep and thermal aging at 700 C. *Materials Science and Engineering: A*, 711:165–174, 2018.

[18] R Viswanathan and W Bakker. Materials for ultrasupercritical coal power plants—boiler materials: Part 1. *Journal of materials engineering and performance*, 10:81–95, 2001.

[19] JP Shingledecker, ND Evans, and GM Pharr. Influences of composition and grain size on creep–rupture behavior of inconel alloy 740. *Materials Science and Engineering: A*, 578:277–286, 2013.

[20] F Sun, YF Gu, JB Yan, ZH Zhong, and M Yuyama. Phenomenological and microstructural analysis of intermediate temperatures creep in a Ni–Fe-based alloy for advanced ultra-supercritical fossil power plants. *Acta Materialia*, 102:70–78, 2016.

[21] Fazel Yavari and Nikhil Koratkar. Graphene-based chemical sensors. *The journal of physical chemistry letters*, 3:1746–1753, 2012.

[22] Dale AC Brownson, Dimitrios K Kampouris, and Craig E Banks. An overview of graphene in energy production and storage applications. *Journal of Power Sources*, 196:4873–4885, 2011.

[23] Amartya Mukhopadhyay, Fei Guo, Anton Tokranov, Xingcheng Xiao, Robert H Hurt, and Brian W Sheldon. Engineering of graphene layer orientation to at-

tain high rate capability and anisotropic properties in Li-Ion battery electrodes. *Advanced Functional Materials*, 23(19):2397–2404, 2013.

[24] Yi Han, Zhen Xu, and Chao Gao. Ultrathin graphene nanofiltration membrane for water purification. *Advanced Functional Materials*, 23(29):3693–3700, 2013.

[25] Jinhong Du and Hui-Ming Cheng. The fabrication, properties, and uses of graphene/polymer composites. *Macromolecular Chemistry and Physics*, 213(10-11):1060–1077, 2012.

[26] Xiao Huang, Xiaoying Qi, Freddy Boey, and Hua Zhang. Graphene-based composites. *Chemical Society Reviews*, 41(2):666–686, 2012.

[27] Yanwu Zhu, Hengxing Ji, Hui-Ming Cheng, and Rodney S Ruoff. Mass production and industrial applications of graphene materials. *National Science Review*, 5(1):90–101, 2018.

[28] Ken Gall, MF Horstemeyer, Mark Van Schilfgaarde, and MI Baskes. Atomistic simulations on the tensile debonding of an aluminum–silicon interface. *Journal of the Mechanics and Physics of Solids*, 48(10):2183–2212, 2000.

[29] Douglas E Spearot, Karl I Jacob, and David L McDowell. Non-local separation constitutive laws for interfaces and their relation to nanoscale simulations. *Mechanics of Materials*, 36(9):825–847, 2004.

[30] V Yamakov, Erik Saether, Dawn R Phillips, and Edward H Glaessgen. Molecular-dynamics simulation-based cohesive zone representation of intergranular fracture processes in aluminum. *Journal of the Mechanics and Physics of Solids*, 54(9):1899–1928, 2006.

[31] XW Zhou, JA Zimmerman, ED Reedy Jr, and NR Moody. Molecular dynamics

simulation based cohesive surface representation of mixed mode fracture. *Mechanics of Materials*, 40(10):832–845, 2008.

[32] Laurent Guin, Jean L Raphanel, and Jeffrey W Kysar. Atomistically derived cohesive zone model of intergranular fracture in polycrystalline graphene. *Journal of Applied Physics*, 119(24), 2016.

[33] Martin Pumera. Electrochemistry of graphene: new horizons for sensing and energy storage. *The Chemical Record*, 9(4):211–223, 2009.

[34] Mohan SR Elapolu, Alireza Tabarraei, Xiaonan Wang, and Douglas E Spearot. Fracture mechanics of multi-layer molybdenum disulfide. *Engineering Fracture Mechanics*, 212:1–12, 2019.

[35] Alireza Tabarraei, Xiaonan Wang, and Dan Jia. Effects of hydrogen adsorption on the fracture properties of graphene. *Computational Materials Science*, 121:151–158, 2016.

[36] Alireza Tabarraei and Xiaonan Wang. Anomalous thermal conductivity of monolayer boron nitride. *Applied Physics Letters*, 108(18), 2016.

[37] Xiaonan Wang and Alireza Tabarraei. Phonon thermal conductivity of monolayer mos2. *Applied Physics Letters*, 108(19), 2016.

[38] Kaveh Safavigerdini, Koundinya Nouduri, Ramakrishna Surya, Andrew Reinhard, Zach Quinlan, Filiz Bunyak, Matthew R Maschmann, and Kannappan Palaniappan. Predicting mechanical properties of carbon nanotube CNT images using multi-layer synthetic finite element model simulations. *arXiv preprint arXiv:2307.07912*, 2023.

[39] Wjefferson HS Brandão, Acrisio L Aguiar, Alexandre F Fonseca, DS Galvão, and

JM De Sousa. Mechanical properties of tetragraphene single-layer: A molecular dynamics study. *Mechanics of Materials*, 176:104503, 2023.

[40] Bart Partoens and FM Peeters. From graphene to graphite: Electronic structure around the K point. *Physical Review B*, 74(7):075404, 2006.

[41] Andre K Geim and Konstantin S Novoselov. The rise of graphene. *Nature materials*, 6(3):183–191, 2007.

[42] Qun Wei, Guang Yang, and Xihong Peng. Auxetic tetrahex carbon with ultrahigh strength and a direct band gap. *Physical Review Applied*, 13(3):034065, 2020.

[43] Mei Xu, Alireza Tabarraei, Jeffrey T Paci, Jay Oswald, and Ted Belytschko. A coupled quantum/continuum mechanics study of graphene fracture. *International journal of fracture*, 173(2):163–173, 2012.

[44] Bin Zhang, Lanjv Mei, and Haifeng Xiao. Nanofracture in graphene under complex mechanical stresses. *Applied Physics Letters*, 101(12):121915, 2012.

[45] Mohammed A Rafiee, Javad Rafiee, Iti Srivastava, Zhou Wang, Huaihe Song, Zhong-Zhen Yu, and Nikhil Koratkar. Fracture and fatigue in graphene nanocomposites. *small*, 6(2):179–183, 2010.

[46] Fabrício Morais De Vasconcelos, Antônio Gomes Souza Filho, Vincent Meunier, and Eduardo Costa Girão. Electronic properties of tetragraphene nanoribbons. *Physical Review Materials*, 3(6):066002, 2019.

[47] Fabrício Morais de Vasconcelos, Antonio Gomes Souza Filho, Vincent Meunier, and Eduardo Costa Girão. Electronic and structural properties of tetragraphenes. *Carbon*, 167:403–413, 2020.

[48] Babu Ram and Hiroshi Mizuseki. Tetrahexcarbon: A two-dimensional allotrope of carbon. *Carbon*, 137:266–273, 2018.

[49] Mehmet Emin Kilic and Kwang-Ryeol Lee. Tuning the electronic, mechanical, thermal, and optical properties of tetrahexcarbon via hydrogenation. *Carbon*, 161:71–82, 2020.

[50] Mehmet Emin Kilic and Kwang-Ryeol Lee. First-principles study of fluorinated tetrahexcarbon: stable configurations, thermal, mechanical, and electronic properties. *The Journal of Physical Chemistry C*, 124(15):8225–8235, 2020.

[51] Bohayra Mortazavi, Evgeny V Podryabinkin, Ivan S Novikov, Stephan Roche, Timon Rabczuk, Xiaoying Zhuang, and Alexander V Shapeev. Efficient machine-learning based interatomic potentialsfor exploring thermal conductivity in two-dimensional materials. *Journal of Physics: Materials*, 3(2):02LT02, 2020.

CHAPTER 2: Determination of Material Parameters of In740h Under Different Experimental Situations Using Chaboche Model

2.1 Introduction

In this chapter, we present the development and validation of a constitutive model based on the Chaboche approach. This model incorporates both nonlinear isotropic and kinematic hardening rules and is designed to accurately predict the stress-strain behavior of Inconel Alloy 740H. Additionally, we conduct a separate prediction of Inconel 740H's material behavior using only the kinematic hardening rule to highlight any differences in results. Inconel 740H is a high-temperature, nickel-based superalloy celebrated for its remarkable mechanical strength, resistance to creep, and corrosion resilience, making it exceptionally suitable for deployment in extreme environmental conditions.

Our research primarily revolves around two key objectives: the determination of material parameters for the unified Chaboche constitutive model and the validation of its accuracy through experimental data, provided by EPRI, gathered from uniaxial strain-controlled loading tests. These tests encompass a broad temperature range, stretching from room temperature to 600°C, and include strain ranges varying from 0.375% to 0.5%. The outcomes of this research demonstrate the model's effectiveness in capturing the intricate mechanical behavior of Inconel Alloy 740H under diverse conditions.

Inconel 740, a nickel-based superalloy distinguished by its exceptional mechanical and corrosion-resistant properties, has gained considerable prominence across various industries, including aerospace, gas turbines, nuclear reactors, and petrochemicals. Its distinct characteristics render it a great candidate for use in high-temperature and

high-stress environments, where components operate under demanding conditions.

Developing a material model for Inconel 740 holds great importance, as it enables a comprehensive understanding of the alloy's performance across various operational conditions. This model, which serves as a robust tool for engineers and researchers, facilitates the precise prediction of the alloy's response to thermal and mechanical loads. This, in turn, supports the design of secure and efficient components. Additionally, a thorough comprehension of the material's behavior is indispensable for optimizing its performance and ensuring the structural integrity of critical components. As the demand for high-performance materials in extreme environments continues to grow, the establishment of a comprehensive material model for Inconel 740 contributes significantly to the progress of engineering and technology. This chapter addresses the critical need for such a material model and presents its development and validation, thereby providing valuable insights into the behavior of Inconel 740 under varying stress and temperature conditions.

Previous studies have employed various techniques to investigate material damage [1, 2, 3, 4]. In this research, we utilize the Chaboche model to construct the material model for Inconel 740. The Chaboche model has gained significant recognition for its capacity to simulate cyclic plasticity, creep relaxation, and hardening. Within this study, we have developed a dual backstress Chaboche constitutive model by utilizing an extensive experimental database obtained under varying conditions. This database includes uniaxial strain-controlled loading tests conducted at a range of temperatures, from room temperature to 600°C, and covers strain ranges from 0.375% to 0.5%. These tests are designed to replicate the material's behavior in conditions that closely resemble actual operational environments.

The validation of the developed material model is carried out by comparing its predictions with experimental data. The effective agreement between the model's predictions and the experimental results provides strong validation, confirming the

accuracy of the developed material model in replicating the mechanical response of Inconel Alloy 740H.

2.2 Chaboche non-linear combined hardening (NLCH) model

The governing equations of the Chaboche model can be written as $\dot{\epsilon_p} =< \frac{f}{Z} >^n \text{sign}(\sigma - x)$ and $f = |\sigma - x| - R - k$ where Z and n are viscous parameters, ϵ_p is the plastic strain, and f represents the model yield criterion. Material yields when f is equal to zero; while $f < 0$ indicates an elastic behavior.

Both kinematic and isotropic hardening are considered in the unified model, where the isotropic hardening rule is represented by:

$$\dot{R} = b(Q - R)\dot{p} \tag{2.1}$$

where R is the drag stress related to the change in yield surface size, and Q and b are isotropic hardening parameters. Q represents the stabilized R value at saturation, and b represents the speed of the saturation.

The non-linear Kinematic hardening rule was originally introduced by Armstrong and Frederick [5] and can be expressed as:

$$\begin{aligned} \dot{x_i} &= C_i(a_i\dot{\epsilon_p} - x_i\dot{p_i}) \\ x &= x_1 + x_2 \end{aligned} \tag{2.2}$$

where i=1,2, x is the back stress, and a and C are kinematic hardening parameters. $\dot{p}$ is the rate of the accumulated plastic strain; which is equal to $2\Delta\epsilon_p$ for each cycle under uniaxial loading. The summation of back stress components is done to provide a better fit to experimental data [6]. Equations (2.1) and (2.2) demonstrate that model variables such as R and x are dependent on the accumulated plastic strain value. The total stress for the elastic-plastic case can be derived by setting $f = |\sigma - x| - R - k$ to the yield point of the material. Therefore, the total stress can be represented as

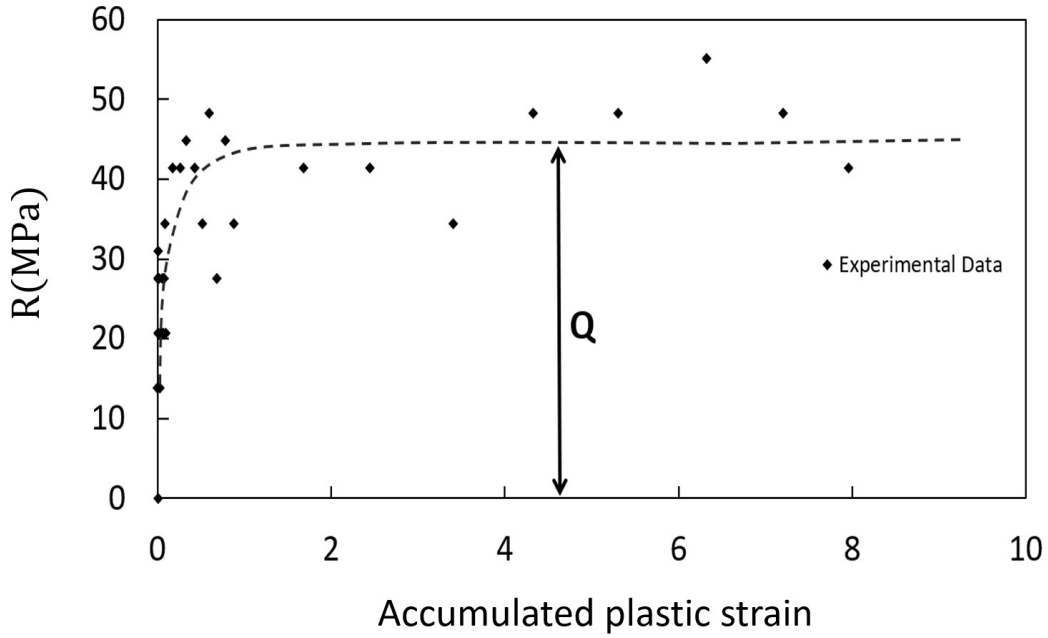

Figure 2.1: Isotropic hardening variable (R) vs accumulated plastic strain (p) for IN740H at 600°C

Table 2.1: Initial Parameters

Temperature(°C)	Strain Range (%)	a_1(MPa)	C_1	a_2(MPa)	C_2	b
20	0.5	0.0096	6730.4	56.54	1928.3	27.61
20	0.375	0.0096	6730.4	56.54	1928.3	27.61
600	0.5	0.0161	2950.8	74.05	1105	22.68
600	0.375	0.0042	7261.3	63.43	1921.9	14.66

follows

$$\sigma = x + (R + k)\text{sign}(\sigma - x) = E(\epsilon - \epsilon_p) \tag{2.3}$$

The current model includes six time-independent material properties, which are kinematic hardening parameters a_1, a_2, C_1, C_2; isotropic hardening parameters b and Q (which is related to b according to Eq. (2.4)). The process used to determine these parameters is discussed in the next section.

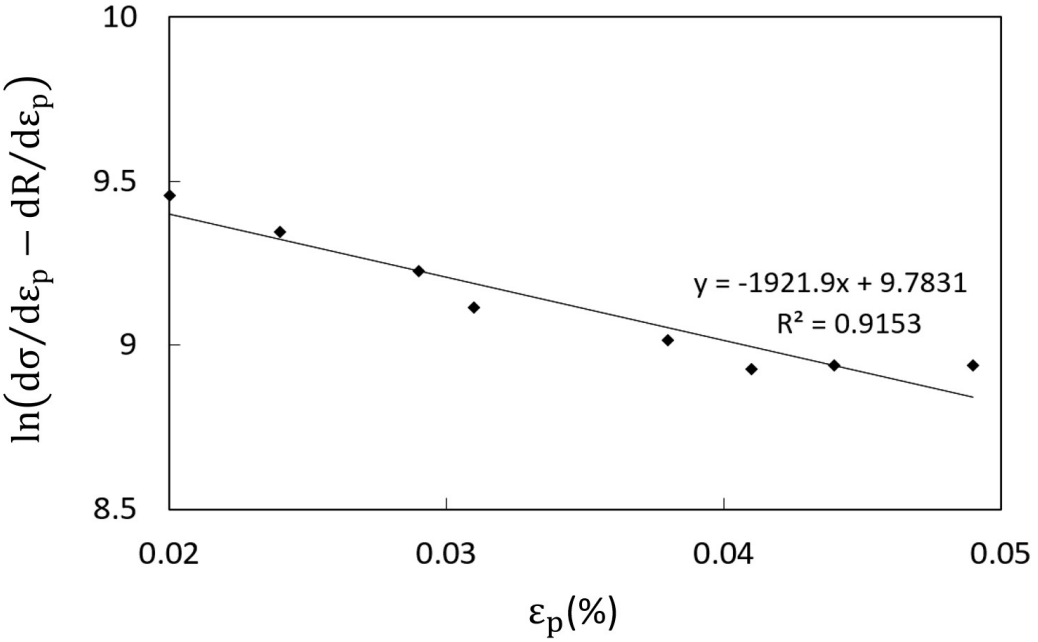

Figure 2.2: Computing kinematic hardening constants a_2 and C_2 for Inconel Alloy 740H at 600°C

2.3 Material parameter determination using NLCH model

2.3.1 Estimation of the initial material parameters

An accurate and rational estimation of the initial material parameters is necessary to accurately fit numerical results to experimental data. Otherwise, the resulting parameters would lack physical validity, even if the numerical results appear to match experimental data. We estimate the initial values of isotropic and kinematic hardening by utilizing an approach similar to that developed by Tong et al. [7, 8]. The integration of Eq. (2.1) results in the evolution of isotropic hardening given by:

$$R = Q(1 - e^{-bp}) \tag{2.4}$$

From Eq. (2.4), it is clear that Q is the saturated value of R, as p increases. Figure 2.1 shows the change in the R values by increasing the accumulated plastic strain, p, from which the value of Q could be determined.

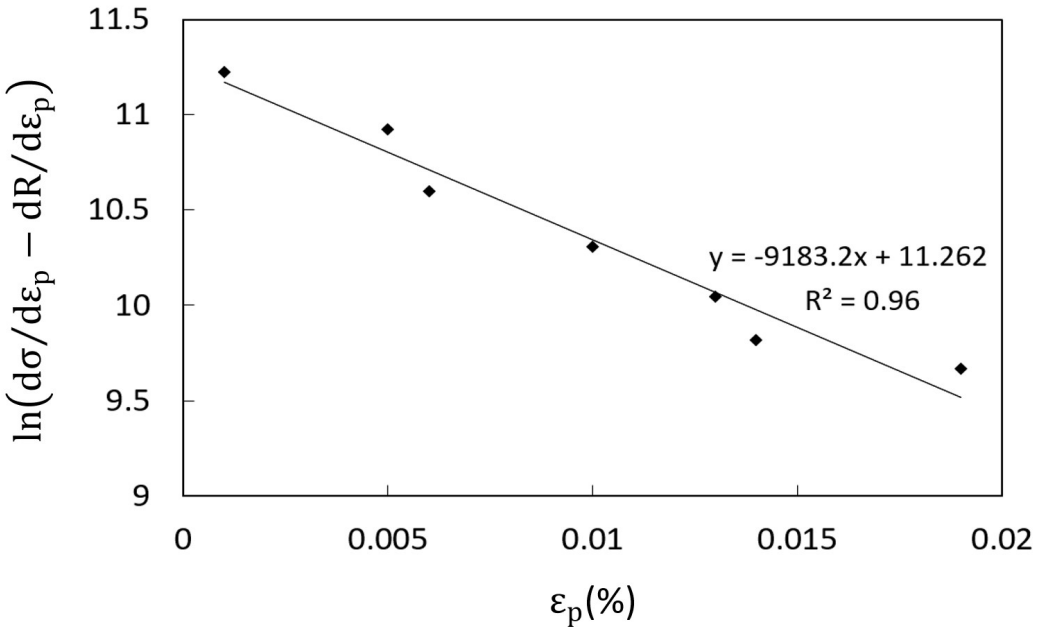

Figure 2.3: Computing kinematic hardening constants a_1 and C_1 for Inconel Alloy 740H at 600°C

The rearrangement of Eq. (2.4) results in the equation for b:

$$b = -\frac{\ln(1 - \frac{R}{Q})}{p} \tag{2.5}$$

The corresponding R and p values can be identified by evaluating a point located in the transient region of the hardening region. Similarly, b is calculated using Eq. (2.5) and the identified Q value.

The initial kinematic hardening parameters, C_i and a_i, are estimated using the initial tensile curve (first-quarter cycle). The integrated form of Eq. (2.2) yields equations for x_1 and x_2, as shown below:

$$\begin{aligned} x_1 &= a_1(1 - e^{-C_1\epsilon_p}) \\ x_2 &= a_2(1 - e^{-C_2\epsilon_p}) \end{aligned} \tag{2.6}$$

Substituting Eq. (2.6) into Eq. (2.2) and then into Eq. (2.3) gives:

$$\sigma = a_1(1 - e^{-C_1\epsilon_p}) + a_2(1 - e^{-C_2\epsilon_p}) + R + k \tag{2.7}$$

In the later stages of hardening, the influence of x_1, and hence a_1 and C_1, to hardening is negligible. As a result, the later stages of kinematic hardening are mainly governed by x_2, a_2, and C_2. Therefore, for these stages, Eq. (2.7) can be written as:

$$\sigma = a_2(1 - e^{-C_2\epsilon_p}) + R + k \tag{2.8}$$

By differentiating Eq. (2.8) with respect to ϵ_p, assuming that the yield stress, k, is constant, and taking the natural logarithm of both sides, Eq. (2.8) can be expressed in the following form:

$$\ln(\frac{\partial\sigma}{\partial\epsilon_p} - \frac{\partial R}{\partial\epsilon_p}) = -C_2\epsilon_p + \ln(a_2C_2) \tag{2.9}$$

Figure 2.2 shows the plot of $\ln(\frac{\partial\sigma}{\partial\epsilon_p} - \frac{\partial R}{\partial\epsilon_p})$ versus ϵ_p at a larger plastic strain range. By using Eq. (2.9), C_2 and a_2 are identified by fitting a regression line through the data points on this plot. Subsequently, the values of C_1 and a_1 can be determined for the transient region from Eq. (2.7). This yields the following equation:

$$\ln(\frac{\partial\sigma}{\partial\epsilon_p} - \frac{\partial R}{\partial\epsilon_p}) = -(C_1 + C_2)\epsilon_p + \ln(a_1C_1) + \ln(a_2C_2) \tag{2.10}$$

Figure 2.3 shows the plot of $\ln(\frac{\partial\sigma}{\partial\epsilon_p} - \frac{\partial R}{\partial\epsilon_p})$ versus ϵ_p at lower plastic strain range, based on Eq. (2.10). The initial parameters obtained from this method are presented in Table 2.1.

Table 2.2: Optimized Parameters

Temperature(°C)	Strain Range (%)	a_1(MPa)	C_1	a_2(MPa)	C_2	b
20	0.5	62	657	80	650	4
20	0.375	61	753	93	704	10
600	0.5	82	820	35	701	10
600	0.375	75	950	36	1400	20

2.3.2 Optimization of the parameters

In the preceding section, we established initial estimates for the material parameters. These estimations serve as inputs for the optimization process, aiming to derive the most favorable values from experimental data. To achieve this, we utilize both the initial ten cycles and randomly selected cycles as inputs. Subsequently, we repeat the entire optimization process for ten epochs.

Several optimization methods are available to optimize the data. In this study, a non-linear least-squares algorithm has been selected as the optimization method. This method aims to find the global minimum difference between the stresses derived from the unified Chaboche model and the stresses obtained from the experimental data under strain control conditions [9]. The objective function used for this purpose is outlined below:

$$F(x) = \sum [\sigma(x)_i^{num} - \sigma_i^{exp}]^2 \tag{2.11}$$

$$x \in R^n \tag{2.12}$$

$$LU \leq x \leq UB \tag{2.13}$$

where x is the optimization variable, which is an n-dimensional space vector, R^n (n=5 in this study). In the current case, x includes the following material constants

in the Chaboche model.

$$x = [a_1, C_1, a_2, C_2, b]^T \tag{2.14}$$

In the optimization procedure, it is necessary to define the lower and upper boundaries of the variable x, which are referred to as LB and UB, respectively. The terms $\sigma(x)_i^{num}$ and σ_i^{exp} represent the numerical and experimental total stress, respectively, and i denotes the total number of experimental data points.

2.3.3 Numerical method

The total numerical stress is determined by solving the system of equations, Eq. (2.1) to Eq. (2.4), concerning the known material constants. Several mathematical algorithms have been developed to predict the system's state [10, 11]. Here, the Newton-Raphson method is used as a numerical method for solving the system of equations. This method involves assuming an initial value for the unknown variable (as shown in Eq. (2.15)) and then updating the variable approximation using Eq. (2.16).

$$X_n = X_{initial} \tag{2.15}$$

$$X_{n+1} = X_n - \frac{f(X_n)}{f'(X_n)} \tag{2.16}$$

$$\text{tol} = |1 - \frac{X_n}{X_{n+1}}| \tag{2.17}$$

where X is an unknown variable, and f is the zero-form function corresponding to the X variable. This process is repeated until the tolerance, as defined by Eq. (2.17), becomes less than the specified value.

2.4 Material parameter determination using NLKH model

The non-linear kinematic hardening (NLKH) Chaboche model is recognized as one of the most popular models among various models designed to describe the behavior of

materials. Its popularity arises from the fact that deriving the constitutive coefficients required to apply the NLKH model is simple, as they can be obtained from cyclic stress-strain tests. In this study, an NLKH Chaboche model is developed with two back stresses to capture the hardening behavior of the material during cyclic loading. The definition of the back stress evolution in the NLKH model is as follows:

$$dx = \frac{2}{3} C \, d\epsilon^{p} - a \, x \, dp \tag{2.18}$$

The NLKH coefficients are determined by utilizing Eq. (2.19) which is the integrated expression of Eq. (2.18) over a stable strain-controlled response.

$$\frac{\sigma}{2} - k = \frac{C_i}{a_i} \tanh\left(a_i \frac{\Delta \epsilon^{pl}}{2}\right) \tag{2.19}$$

where i represents the number of back stresses used to describe the material. Material coefficients are defined manually by fitting the NLKH model to the experimental data. For this purpose, the initial values obtained in the previous section are used as the initial guess.

The initial step in this procedure involves acquiring the stable response of the material through experimentation. Once the stable response is determined, the values for σ_a, ϵ_a, k, and ϵ_p can be readily identified. Moreover, to establish the material constants for the Chaboche NLKH model, determining the value for k is essential. The theory defines k as the initial departure from linearity. However, it does not specify a definitive plastic strain value for this deviation, with various sources suggesting that this value may be notably lower than the conventional 0.2% used for the yield criterion. In this study, the deviation from linearity is defined as $\epsilon_p = 10^{-5}$. The process of fitting the Chaboche NLKH parameters is divided based on the number of backstresses selected. For example, Figure 2.8 illustrates how two sets of the Chaboche NLKH parameters are utilized to fit the test data for the pristine material

at 400°C. This is accomplished by selecting trial values for the parameters a_i and C_i and plotting the stress response for a theoretical range of plastic strain. The parameters are optimized to closely match the trial data sum. As depicted in Figure 2.8, the parameters for $i = 1$ and $i = 2$ should target different strain regions of the material. This is evidenced by the rapid increase of the curve representing $i = 1$, followed by a leveling off, where the contribution from $i = 2$ becomes more prominent, capturing the slower increase. Additionally, the accuracy of the fit should consider the expected strain range. In this work, it is anticipated that plastic deformation will be small. Hence, the focus lies on accurately fitting the data representing smaller plastic strains. Furthermore, achieving a perfect fit for all data points within each strain range is impractical, as shown in Figure 2.9.

2.5 Numerical and experimental results comparison

The simulated hysteresis loops, generated using the NLCH Chaboche parameters listed in Table 2.2, are validated by comparing them with the corresponding experimental results. Figures 2.4-2.7 show this comparison, presenting the cyclic stress-strain behavior observed during uniaxial loading tests conducted at different temperatures and strain ranges. Specifically, these figures illustrate the first and saturated cycles. The figures provide compelling evidence of a good agreement between the numerical solutions, obtained through parameter optimization, and the experimental data. Moreover, the optimized parameters effectively capture the transient behavior between the first and saturated cycles.

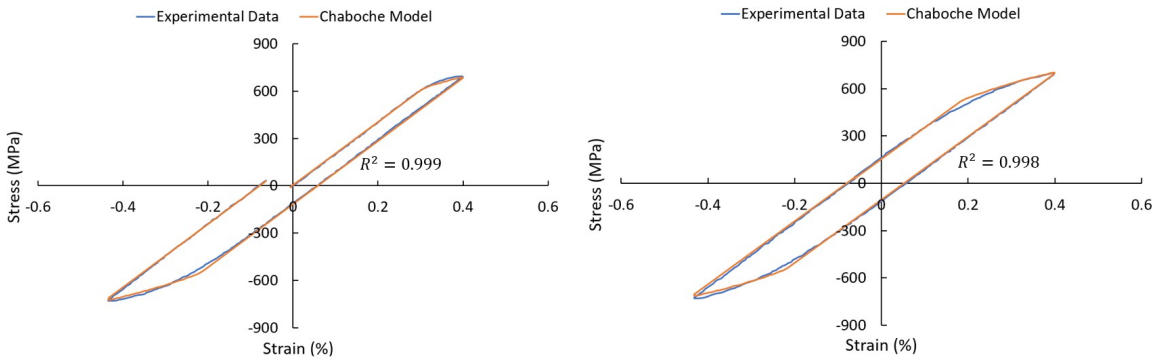

Figure 2.4: NLCH model vs experimental data for 0.5% strain at 20°C; (a) first loop, (b) saturated loop.

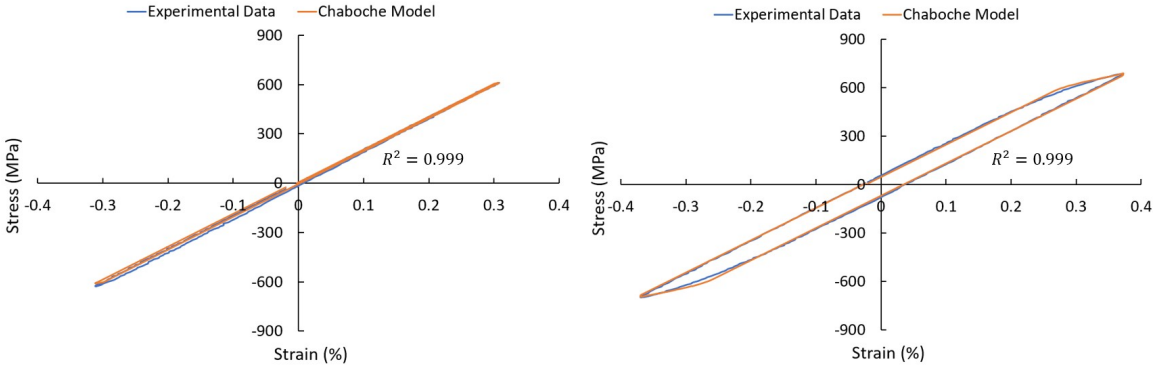

Figure 2.5: NLCH model vs experimental data for 0.375% strain at 20°C; (a) first loop, (b) saturated loop.

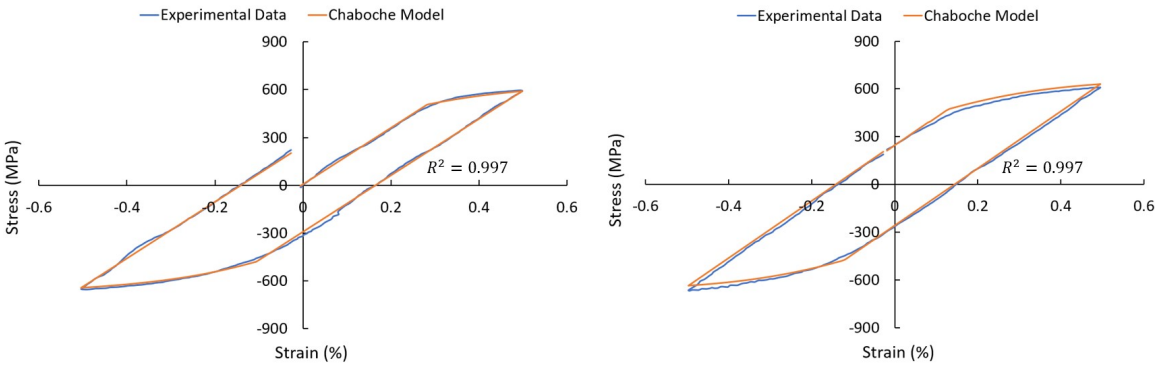

Figure 2.6: NLCH model vs experimental data for 0.5% strain at 600°C; (a) first loop, (b) saturated loop.

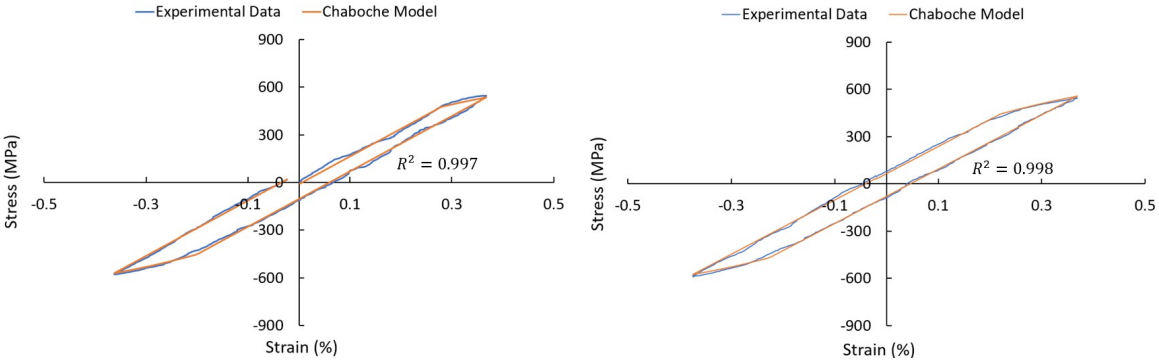

Figure 2.7: NLCH model vs experimental data for 0.375% strain at 600°C; (a) first loop, (b) saturated loop.

To quantify the level of agreement between the numerical data and experimental results, R-squared values are provided. Typically, an R-squared value exceeding 0.9 indicates a strong fit. The R-squared values displayed in Figures 2.4-2.7 indicate a favorable correspondence between the estimated hysteresis loops, obtained using the optimized material parameters, and the experimental loops. Based on these values, it can be concluded that, at the same strain range, there is a higher level of agreement between the numerical data and experimental results at room temperature compared to 600°C. Additionally, the model exhibits better predictive capabilities for smaller strain ranges when considering the same temperature.

On the other side, the strong agreement observed between the NLKH model and experimental data illustrates the feasibility of obtaining Chaboche NLKH model coefficients through a limited number of tests. The final coefficients for the Chaboche NLKH model of the Service-Exposed material are presented in Table 2.4.

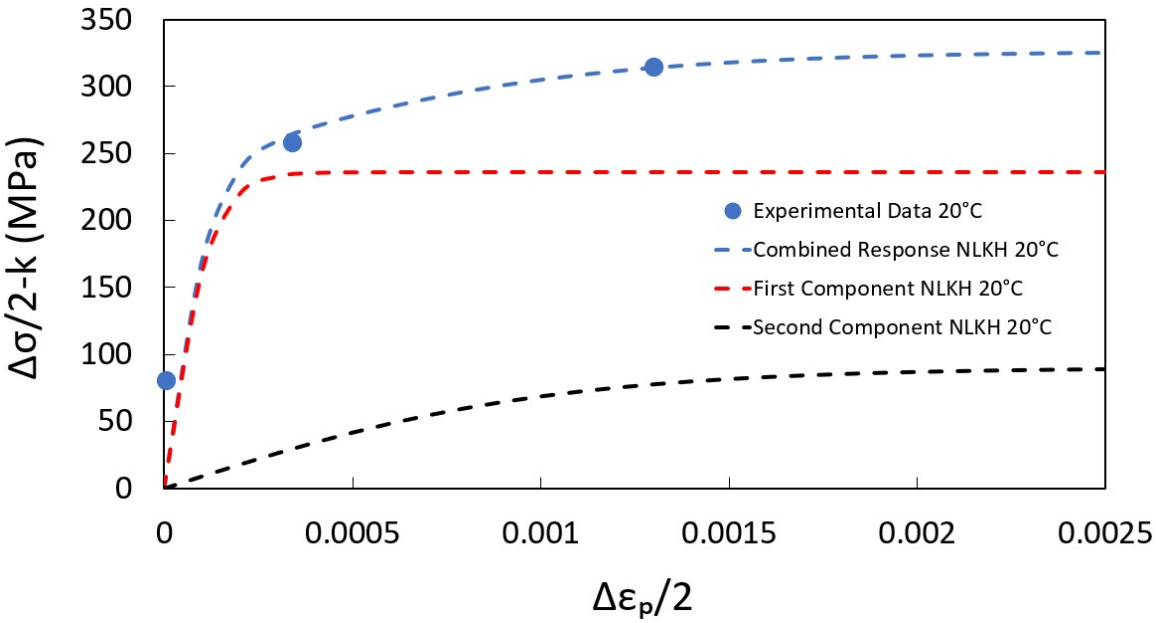

Figure 2.8: Chaboche NLKH data vs. experimental data.

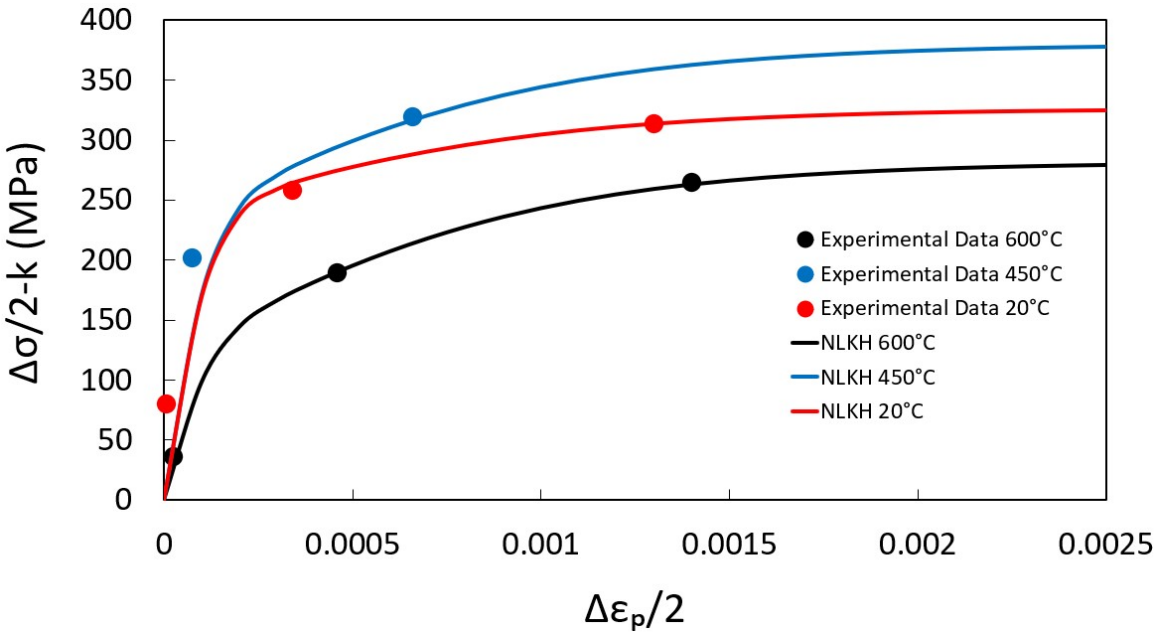

Figure 2.9: Chaboche NLKH data vs. experimental data.

Table 2.3: Initial Parameters

Temperature(°C)	a_1(MPa)	C_1	a_2(MPa)	C_2
20	1	7000	60	2000
450	1	7000	60	2000
600	1	7000	60	2000

Table 2.4: Optimized parameters obtained from NLKH model

Temperature(°C)	a_1(MPa)	C_1	a_2(MPa)	C_2
20	2000	180000	16500	3900000
450	2000	300000	16500	3800000
600	2000	320000	16500	2000000

2.6 Conclusion

In conclusion, this study utilizes both Chaboche NLCH and NLKH models to determine the material parameters that describe the stress-strain behavior in Inconel Alloy 740H. Material model parameters are determined through tensile test experiments performed at different temperatures and strain ranges. Parameter values are estimated directly from the experimental data and optimized using a least-squares algorithm (for the NLCH model). Through a comprehensive comparison of model predictions with experimental data, a strong agreement is observed, validating the proposed model's accuracy in predicting material behavior using two back stresses.

REFERENCES

[1] Alireza Tabarraei, Jeong-Hoon Song, and Haim Waisman. A two-scale strong discontinuity approach for evolution of shear bands under dynamic impact loads. *International Journal for Multiscale Computational Engineering*, 11(6), 2013.

[2] Shank S Kulkarni and Alireza Tabarraei. An ordinary state based peridynamic correspondence model for metal creep. *Engineering Fracture Mechanics*, 233:107042, 2020.

[3] G Venkatramani, S Ghosh, and M Mills. A size-dependent crystal plasticity finite-element model for creep and load shedding in polycrystalline titanium alloys. *Acta materialia*, 55(11):3971–3986, 2007.

[4] Hamid Hajbarati and Asghar Zajkani. A novel finite element simulation of hot stamping process of DP780 steel based on the chaboche thermomechanically hardening model. *The International Journal of Advanced Manufacturing Technology*, 111:2705–2718, 2020.

[5] Peter J Armstrong, CO Frederick, et al. *A mathematical representation of the multiaxial Bauschinger effect*, volume 731. Berkeley Nuclear Laboratories Berkeley, CA, 1966.

[6] Abdullah Aziz Saad. *Cyclic plasticity and creep of power plant materials*. PhD thesis, University of Nottingham, 2012.

[7] Jie Tong, Z-L Zhan, and B Vermeulen. Modelling of cyclic plasticity and viscoplasticity of a nickel-based alloy using chaboche constitutive equations. *International journal of Fatigue*, 26(8):829–837, 2004.

[8] YP Gong, Christopher J Hyde, W Sun, and TH Hyde. Determination of material properties in the chaboche unified viscoplasticity model. *Proceedings of the Institution of Mechanical Engineers, Part L: Journal of Materials: Design and Applications*, 224(1):19–29, 2010.

[9] Rolf Mahnken and Erwin Stein. Parameter identification for viscoplastic models based on analytical derivatives of a least-squares functional and stability investigations. *International Journal of Plasticity*, 12(4):451–479, 1996.

[10] Rajvardhan Nalawade, Arash Nouri, Utkarsh Gupta, Anish Gorantiwar, and Saied Taheri. Improved vehicle longitudinal velocity estimation using accelerometer based intelligent tire. *Tire Science and Technology*, 2022.

[11] Saeed Izadi, Khatereh Jabari, Mahnaz Izadi, Khadem Hamedani Hamedani, and Azad Ghaffari. Identification and diagnosis of dynamic and static misalignment in induction motor using unscented kalman filter. pages 155–160, 2021.

CHAPTER 3: Hybrid finite element-molecular dynamics study of the fracture behavior of polycrystalline graphene

3.1 Introduction

This chapter explores the mechanical properties of polycrystalline graphene from nanoscale to macroscales by utilizing multiscale molecular dynamics (MD)–finite element (FE) modeling. The investigation of the nanoscale part involves using MD simulations to study the crack propagation and the mechanical behavior of the polycrystalline graphene sheet. However, due to the limitations of atomic-level simulations, modeling the behavior of the large scale polycrystalline is not possible by using MD simulations. Therefore, other methods such as FE analysis are needed to model crack initiation and growth in such systems. To achieve this, a multiscale modeling approach is adopted. Initially, MD simulations are utilized on bicrystalline graphene sheets with different grain boundaries (GB) and atomic structures under uniaxial tension loading. These simulations are conducted to extract the local elastic properties of GBs using a cohesive zone model. Subsequently, the local properties derived using MD are incorporated into FE simulations, which enables the modeling of large scale polycrystalline graphene sheets considering the effect of the grain boundaries. The grains are modeled as pristine graphene, and the simulations are repeated with varying grain sizes to investigate their impact on mechanical properties such as Young's modulus and fracture stress. The results reveal a significant relationship between the grain size and the mechanical properties of polycrystalline graphene, indicating a crucial role of the grain size in its behavior.

A fundamental understanding of the mechanical behavior of the materials is of great importance to use them safely in aerospace, automobile, electronics, nuclear

power, and chemical industries. Many components in these industries are subjected to thermo-mechanical fatigue (TMF) loads and are working under high temperature and pressure conditions[1, 2, 3, 4, 5]. Therefore, the safe structural design of such components is complicated due to the several life-limiting mechanisms interacting and contributing simultaneously to the failure. Hence, understanding the material behavior under this condition is necessary to estimate the lifetime of the components and have a safe design. Among the materials used in the industry, graphene is considered a great candidate material for many applications [6, 7, 8, 9, 10, 11] due to its extraordinary features, therefore, studying the mechanical properties and fracture mechanism of the graphene is vital. To this end, we are investigating the fracture behavior of the polycrystalline graphene sheets and the effect of the grain size on their mechanical properties from nanoscale to macroscales.

This research aims to answer a fundamental question: how is it possible to model the mechanical behavior of the polycrystalline graphene sheet and find its material properties on a large scale. While many companies became interested in pursuing large scale polycrystalline graphene sheets [12] in industry, there is still a lack of knowledge in multiscale modeling of polycrystalline graphene on a large scale. Modeling the behavior of the large scale polycrystalline is not possible by using molecular dynamics (MD) simulations because of the limitations in the atomic level simulations, and it demands utilizing other methods such as the finite element analysis (FEA) to model crack initiation and growth. To achieve this, one way is using cohesive zone models and extraction of the cohesive laws through experimental work, which is challenging. Many atomistic simulations are conducted to extract the cohesive laws, but in all of them, only one or two grain boundaries are considered, while to model the behavior of the polycrystalline graphene by using the cohesive laws, it is necessary to include different grain boundaries with different atomic structures.

In this study, to answer the above-mentioned question, we are conducting a multiscale

analysis using finite elements and MD simulations to study the crack propagation and the mechanical behavior of the polycrystalline graphene sheet on a large scale. As mentioned, large scale polycrystalline graphene sheets have received noticeable attention in industries while there is a lack of knowledge in this area, thus, multiscale modeling of their fracture behavior is of high importance and still challenging due to the extracting cohesive laws of different grain boundaries with different atomic structure from MD simulations and utilizing them in finite element analysis. In this research, we are studying the multiscale modeling of polycrystalline graphene on a large scale for the first time. The cohesive laws are extracted from different grain boundaries, and the results are implemented in Finite element simulations to investigate the effect of the grain size on the mechanical behavior of the large scale polycrystalline graphene sheet. These findings would have significant outcomes for the mass production of graphene materials for industrial applications.

3.2 Computational method

As previously mentioned, the focus of this chapter lies in exploring the effect of grain size on the mechanical properties of polycrystalline graphene from the nanoscale to the macroscale. The overall approach is briefly outlined here, followed by subsequent subsections providing detailed descriptions of each method. For the nanoscale simulations, first polycrystalline graphene sheets with different average grain sizes are created by using a specially developed MATLAB code (MathWorks, Natick, MA, USA), that makes use of the Voronoi tessellation method [13, 14, 15], these 2D sheets are randomly filled with grains. After creating the polycrystalline graphene sheets, MD simulations are conducted to determine Young's modulus and fracture stress under uniaxial tensile loading.

For the larger scales, the MD–FE multiscale simulations are performed. Initially bicrystalline graphene sheets with different GB's misorientation angles are generated by using a MATLAB code (MathWorks, Natick, MA, USA). Subsequently, the bicrys-

talline graphene sheets are subjected to uniaxial tensile loading using MD simulation to extract the local elastic properties of the GBs (interphase region) through a cohesive zone model. These properties are then incorporated into the FE model. Finally, a FE model is created using the generated Voronoi diagrams to represent the polycrystalline graphene sheet. The material properties of the internal grains and the GBs are then included in the FE model based on the derived properties from the MD simulations. The following is a comprehensive explanation of each method.

3.2.1 Description of MD simulations

Comprehensive molecular dynamics (MD) simulations are used to characterize the Young's modulus and fracture strength of polycrystalline, bicrystalline, and pristine graphene on the nanoscale. The freely available Large scale Atomic/Molecular Massively Parallel Simulator (LAMMPS) package is used to conduct MD simulations. To describe the interaction between the carbon atoms, machine learning interatomic potentials (MLIPs) are used. MLIPs are chosen due to their effectiveness and convenience in enabling first principles multiscale modeling using molecular dynamic/finite element simulations. This greatly enhances the computational design capability of novel nanostructures. In other words, MLIPs enable the study of properties in complex microstructures, without the need for prior knowledge about the properties [16].

The system's initial configuration is achieved by minimizing its potential energy by the use of the conjugate gradient method to eliminate any initial internal stress. Following the minimization process, the system undergoes a 50 ps simulation in a microcanonical ensemble (NVE) where the Berendsen thermostat is used. Subsequently, to ensure system stability, the model is annealed in a canonical ensemble (NVT) for 50 ps, gradually raising the temperature to 600 K. This elevated temperature increases the mobility of carbon atoms, enabling the rearrangement of atomic positions. As a result, regions with unusually low or high atomic densities near the grain boundaries are eliminated, leading to further system energy reduction. The

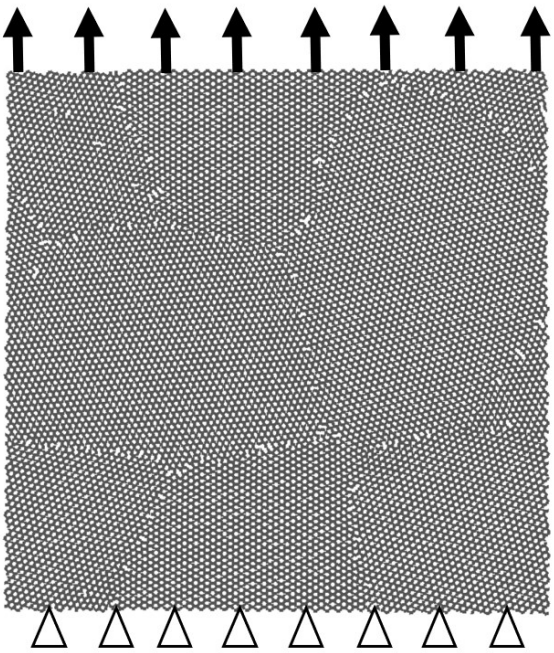

Figure 3.1: Applied boundary conditions on the polycrystalline graphene sheet in MD model.

model is then cooled down to room temperature and equilibrated at 300 K for 10 ps. The equations of motion are integrated using the velocity Verlet scheme.

3.2.1.1 Polycrystalline graphene

All the polycrystalline graphene sheets have the same dimension of 20 $\times$ 20 nm with average grain sizes varying between 2.7 to 10.3 nm. Two parallel reflective walls are positioned at a distance of 0.3 nm in the z-direction to restrict the out-of-plane displacement while allowing for unrestricted 3D local motion of the atoms. These constraints have no impact on the quantitative observations obtained from the simulations or the qualitative behavior of the fracture process at the interface of the bi-material [17].

The simulation samples undergo displacement-controlled uniaxial tension deformation, where the domain is stretched in the y-direction while allowing relaxation in the lateral directions. This deformation is conducted under constant temperature, pressure, and strain rate conditions. Throughout the loading process, the forces act-

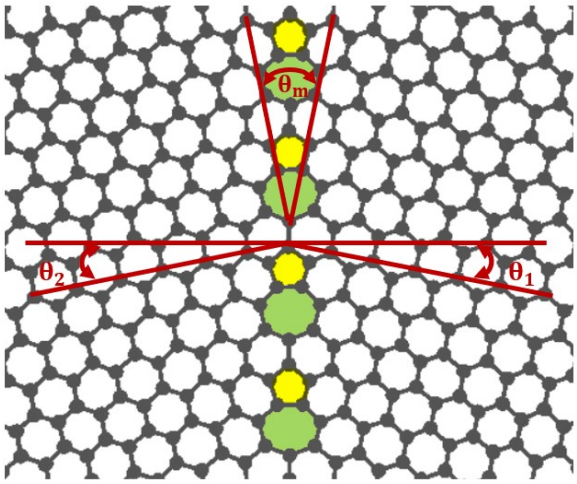

Figure 3.2: Representation of the misorientation angle θ_m of the grain boundary (GB).

ing on a strip of atoms at the top and bottom edges of the panel have their y and z-components set to zero to restrict movement in those directions while enabling free movement in the x-direction. Figure 3.1 represents the boundary condition applied on the polycrystalline graphene sheet.

3.2.1.2 Bicrystalline graphene

Bicrystalline graphene sheets including GBs in the y-direction with different misorientation angles varying between 7.3 and 32.2 degrees are created to extract the local elastic properties of the GBs through a cohesive zone model. To model the behavior of the polycrystalline graphene by using the cohesive laws, it is necessary to include different grain boundaries with different atomic structures.

The identification of GBs relies on two angles, θ_1 and θ_2, which describe the orientation of the normal vector of the GB in each grain concerning the zigzag direction, as depicted in Figure 3.2. The misorientation angle, $\theta_m = \theta_1 + \theta_2$, signifies the relative orientation between the two pristine grains.

During the MD simulations, all samples experience displacement-controlled uniaxial tension deformation, in which the model is stretched in the x-direction while relaxation is permitted in the lateral directions. This deformation takes place under

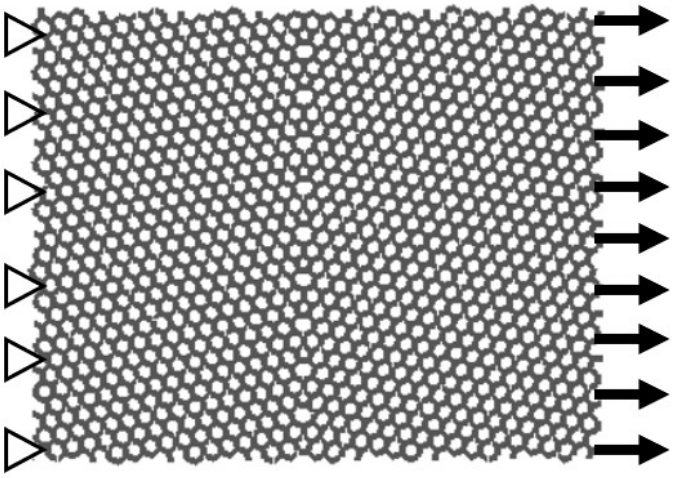

Figure 3.3: Applied boundary conditions on the bicrystalline graphene sheet in MD model.

constant temperature, pressure, and strain rate conditions. Across the loading process, the forces applied to the strip of atoms at the right and left edges of the panel are constrained to have zero x and z-components, effectively restricting movement in those directions while allowing free movement in the y-direction. As an illustration, Figure 3.3 depicts the boundary condition applied on the bicrystalline graphene sheet.

3.2.1.3 Pristine graphene

To determine the material properties of pristine graphene, including the Young's modulus and plastic properties, a 5×5 graphene sheet is subjected to displacement-controlled uniaxial tension deformation. For more accurate results regarding the Young's modulus, the model undergoes stretching first in the y-direction and then in the x-direction. The loading conditions for deformation in the y-direction and x-direction are the same as those used for polycrystalline and bicrystalline models, respectively. The average results from both simulations are then used as the material properties of the pristine graphene, which are subsequently incorporated into the FE model.

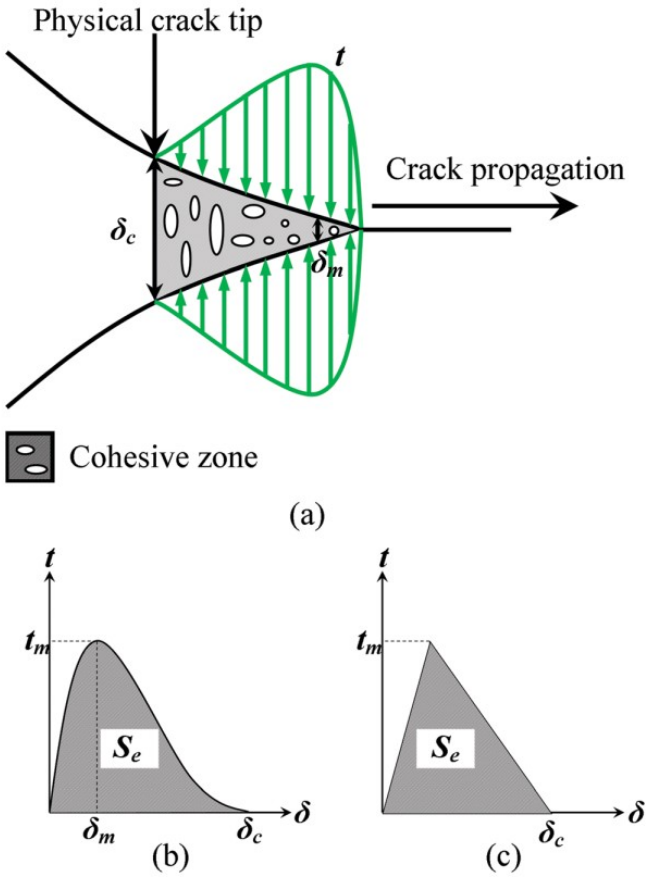

Figure 3.4: (a) Diagram depicting the cohesive zone in front of the crack where cohesive traction t associated with the crack openings d is illustrated. (b) Characteristic profile of a TSL within the Cohesive Zone Model. (c) A typical bilinear TSL [17].

3.2.2 Cohesive zone model

A cohesive zone model (CZM) is applied to extract the local elastic properties of the GBs from MD simulations conducted on the Bicrystalline graphene sheets. CZM is extensively utilized in finite element modeling for explaining local fracture [18, 19]. Barenblatt and Dugdale initially introduced the idea of a cohesive zone model. They achieved this by utilizing the traction on areas close to the crack's tip to represent cohesive forces. Cohesive zone models include a region just ahead of the crack's tip, where the thickness diminishes. Within this area, two cohesive surfaces undergo cohesive traction, as depicted in Figure 3.4a. Within the cohesive zone, the displacement changes discontinuously, and the traction on the cohesive surfaces is a function of the displacement variations between these zones. The cohesive traction that keeps the cohesive surfaces connected can be explained based on the separation between the surfaces. This relationship is shown using a traction–separation law (TSL), which is also known as a cohesive law. A common example of a TSL is displayed in Figure 3.4b.

Various types of cohesive laws, such as bilinear, trapezoid, sinusoidal, and exponential, have been suggested and employed to simulate crack initiation and growth. In this study, the bilinear cohesive law, Figure 3.4c, is chosen for the traction-separation curves derived through MD simulations. This law can be mathematically expressed as:

$$t = \begin{cases} \dfrac{t_m}{\delta_m}\delta & 0 \le \delta \le \delta_m \\ \dfrac{t_m}{\delta_c - \delta_m}(\delta_c - \delta) & \delta_m \le \delta \le \delta_c \\ 0 & \delta \ge \delta_c \end{cases} \tag{3.1}$$

here, t_m stands for the maximum cohesive traction, while δ_c represents the critical

separation. The maximum cohesive traction, t_m, signifies the cohesive strength and appears at δ_m, which denotes the distance of separation where the irreversible failure process begins [20]. The critical displacement, δ_c, indicates the distance between the surfaces where there is no cohesive traction.

The cohesive energy density, S_e, illustrates the amount of work needed to separate the cohesive surfaces per unit area, which is determined by:

$$S_e = \frac{1}{2} t_m \delta_m \tag{3.2}$$

The cohesive traction acting on the cohesive zone is equal to the x-component of the Cauchy stress σ_{xx} derived from the MD simulations. The separation distance is calculated as the average distance between the centroids of the strip of atoms located on the right and left sides of the GB. Since this study focuses on a crack path along the grain boundary, the strip of atoms is centered at the grain boundary line. The separation distance is represented as $\delta = d - d_o$, where d and d_o stand for the distances between the centroids of the atom strip on the right and left sides of the GB in the initial and final configurations, respectively.

In the current study, for the application of CZM in FE modeling, contact cohesive behavior is chosen over the conventional cohesive elements. It assumes a linear elastic traction-separation law before damage. This decision is influenced by assuming a negligible thickness for the GBs in all FE models. Contact cohesive behavior is particularly suitable when the interface's thickness is extremely small. If the interface's adhesive layer has a finite thickness, using conventional cohesive elements might be more suitable for modeling the local fracture.

3.2.3 Description of FE simulations

A novel coupled MD–FE model is utilized in this study to characterize the Young's modulus and fracture strength of polycrystalline graphene sheets on a larger scale,

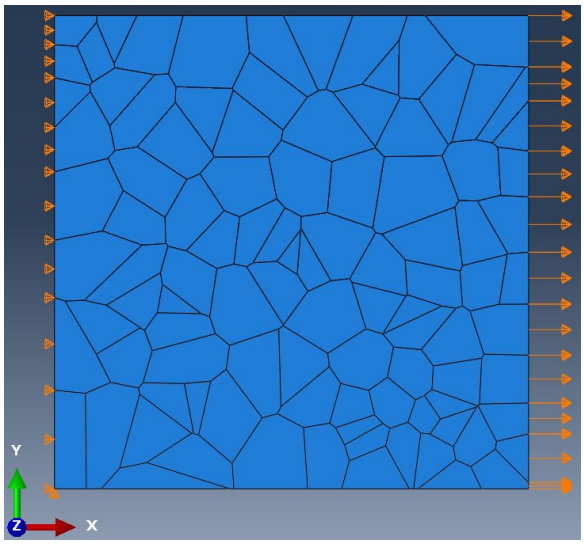

Figure 3.5: Applied boundary conditions on the polycrystalline graphene sheet in FE model.

which bridges the gap between atomistic and continuum methods. This aim is accomplished by incorporating elastic properties of pristine graphene and GBs derived from the MD simulations into a corresponding continuum-based FE model. As previously mentioned, this study concentrates on investigating the influence of grain size on mechanical properties, therefore according to the grain size parameter, a particular number of nucleation sites were randomly allocated within a two-dimensional square-shaped domain. By assuming a square shape for simplification, one can determine the average grain size, denoted as S_g, using the subsequent equation:

$$S_g = \sqrt{\frac{L_s^2}{N_g}} \tag{3.3}$$

here, L_s represents the length of each side, while N_g corresponds to the overall number of grains within the graphene sheet.

The FE model was created using the generated polycrystalline graphene sheets, which were subsequently imported into the ABAQUS FE package. The appropriate loading and boundary conditions were assigned, as depicted in Figure 3.5. All FE models of the polycrystalline graphene sheets were discretized by utilizing the 4-node

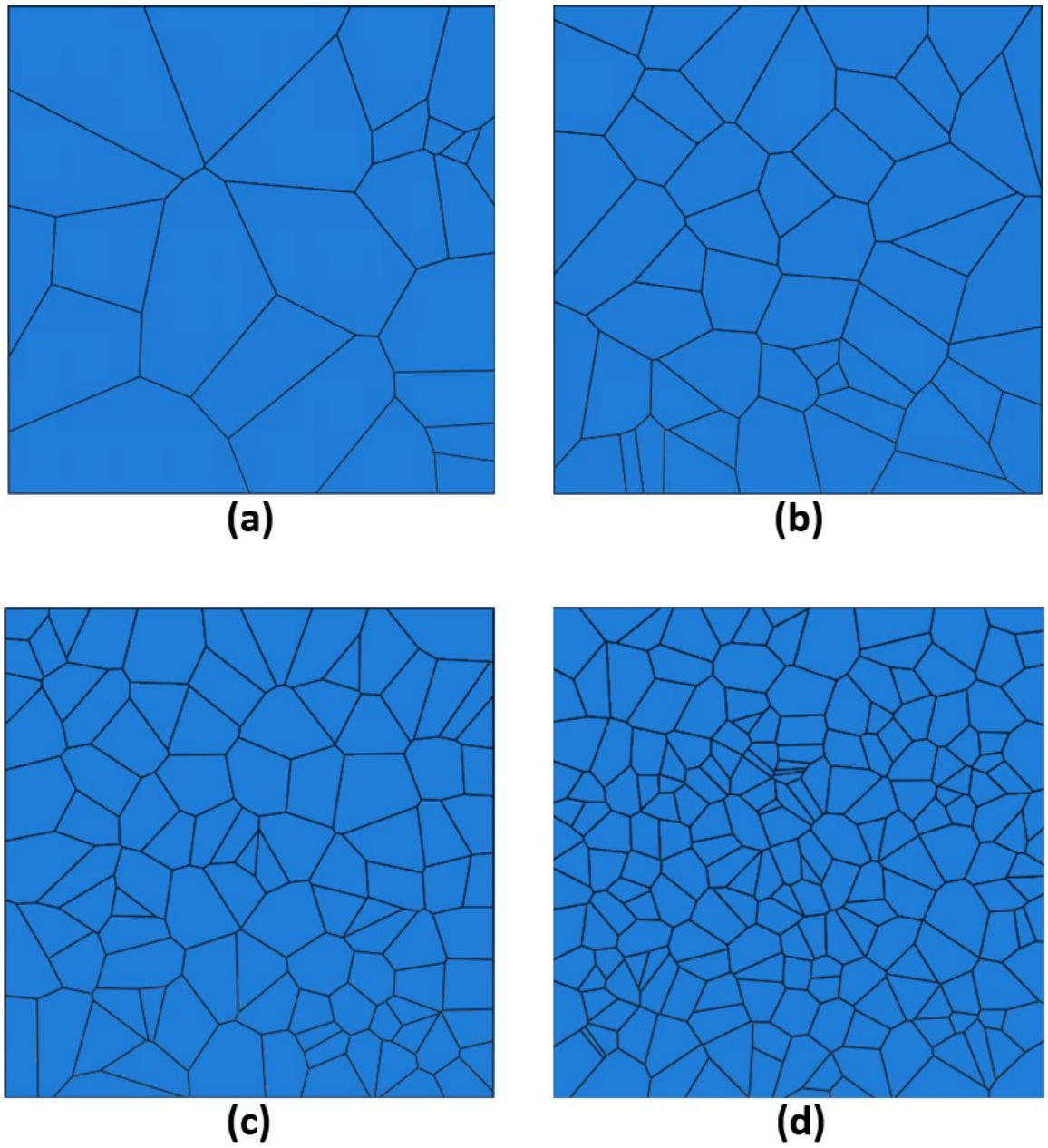

Figure 3.6: FE models used to model polycrystalline graphene sheets with varied average grain sizes.

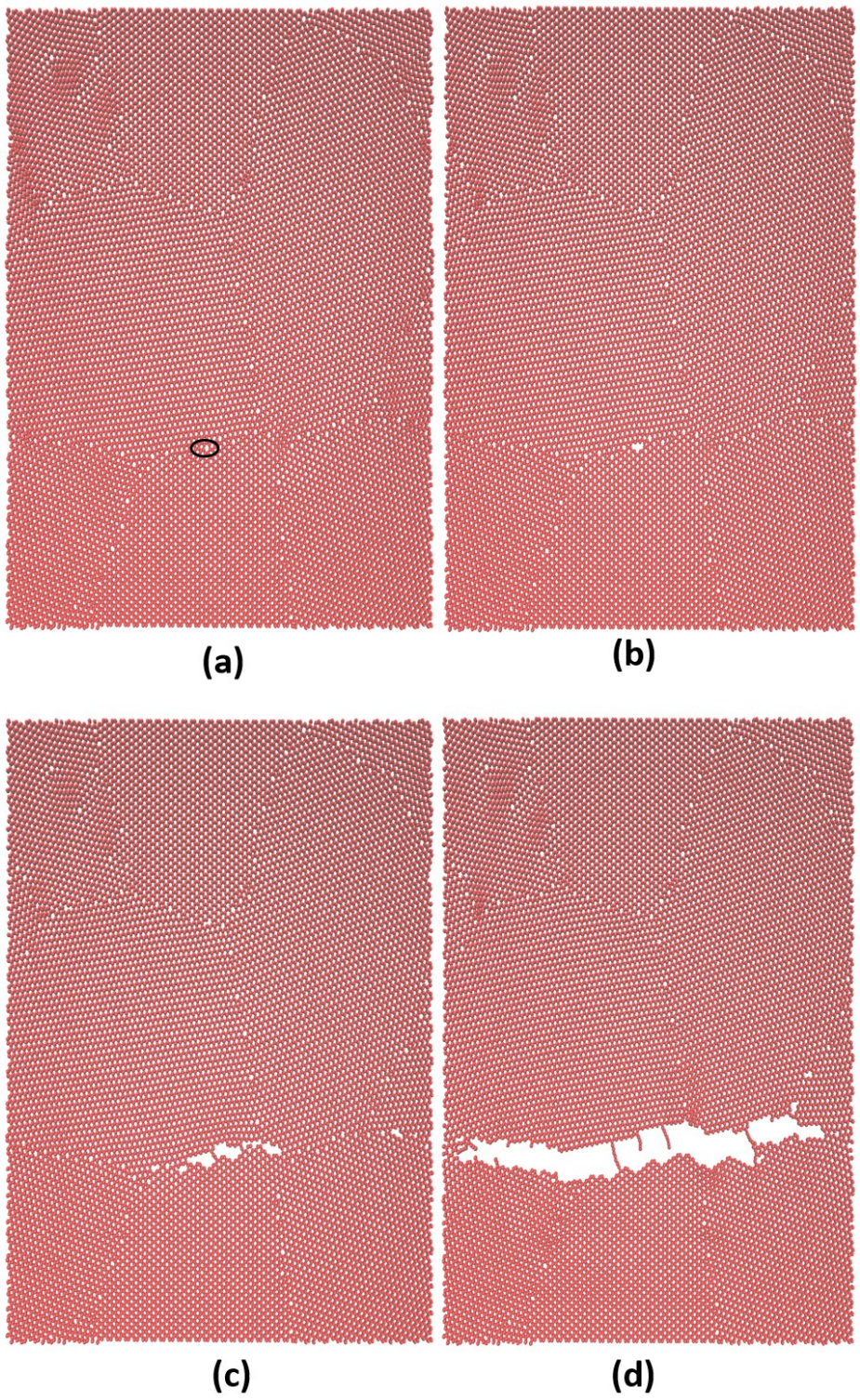

Figure 3.7: Crack propagation path in a polycrystalline graphene sheet.

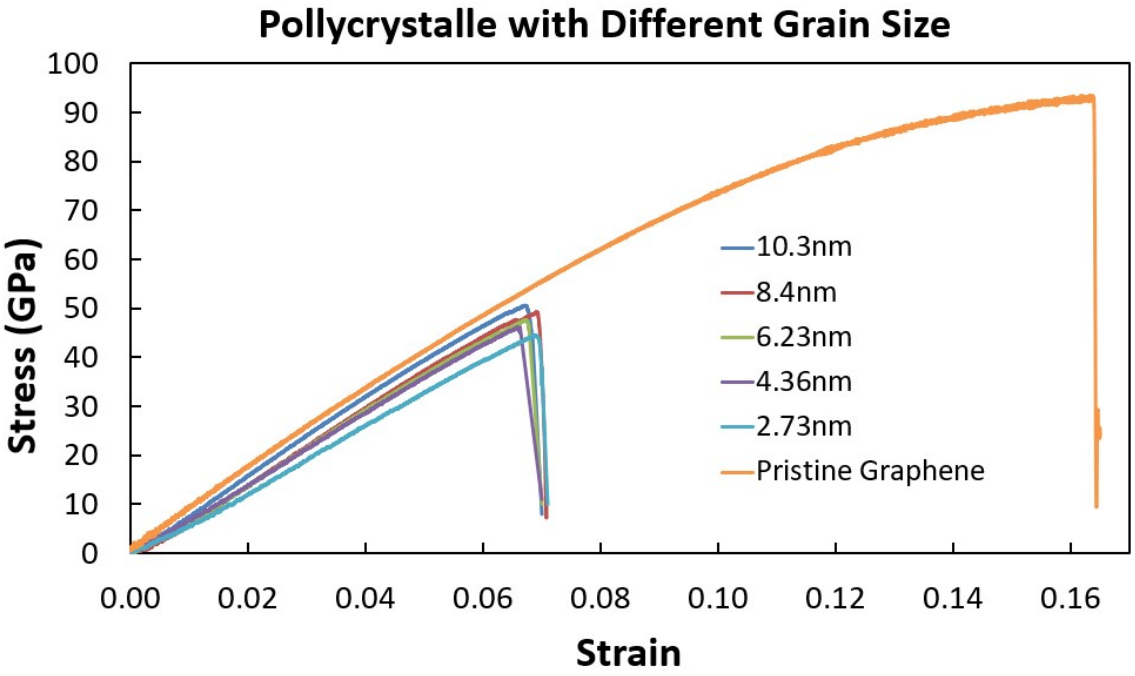

Figure 3.8: Stress-strain curves for the polycrystalline graphene sheets with different grain sizes.

quadrilateral bilinear (PLANE182) plane stress element with reduced integration.

Due to the six-fold rotational symmetry of the atomic lattice in graphene, isotropic linear elastic mechanical properties were attributed to both the pristine graphene and GBs [21, 22].

In the developed FE models, an elastic modulus of 857 GPa, derived from the MD simulations conducted in the previous section, is assigned to the internal grain regions. The Poisson's ratio of graphene was taken to be 0.17 [23]. Moreover, the mechanical properties of the GBs within the FE models were obtained from both the MD simulations and CZM described in the earlier section. Contact cohesive behavior is defined as a surface interaction property. It can be used to model the delamination at interfaces directly in terms of traction versus separation. Specifying a damage model for the contact cohesive behavior allows for the modeling of a bonded interface that may fail as a result of the loading. This modeling approach is an alternative to using cohesive elements or other element types that directly discretize the cohesive

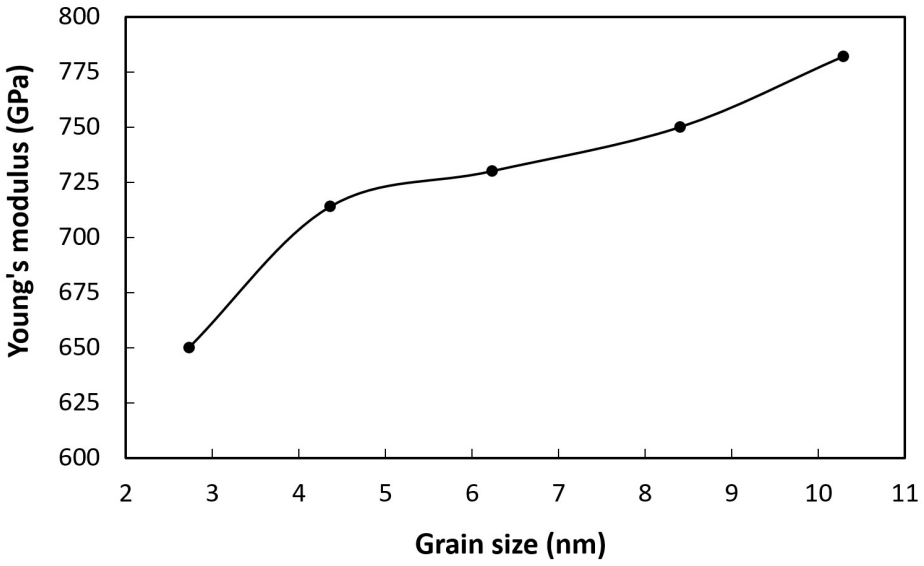

(a)

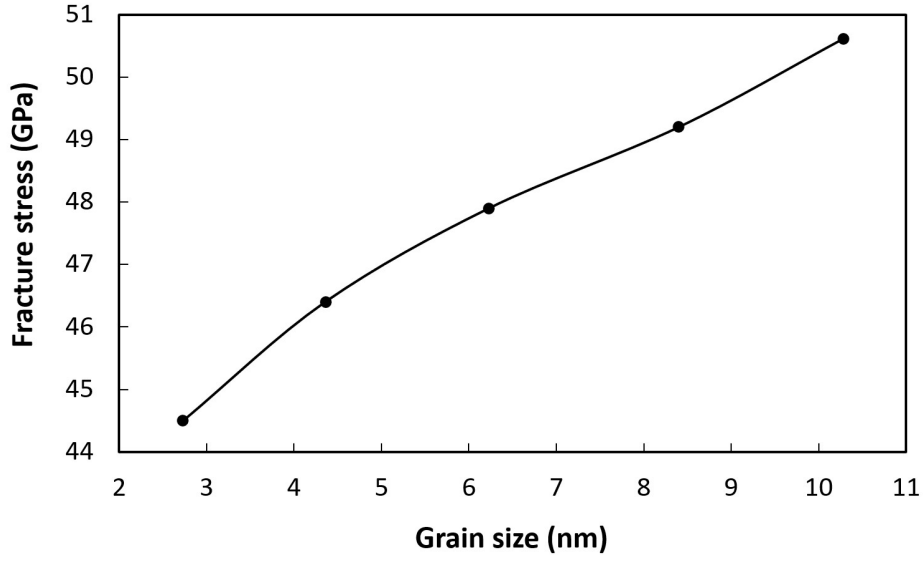

(b)

Figure 3.9: Correlations between the mechanical properties and the average grain size in polycrystalline graphene from MD simulations. (a) Young's modulus, (b) fracture stress as a function of grain size.

material for the simulation.

Similar to the boundary conditions used in the MD simulations, a uniform displacement controlled uniaxial tension was employed at one side of the FE model where the domain is stretched in the x-direction, while the opposite side was kept fixed, as illustrated in Figure 3.5. Throughout the simulation, the instantaneous position of the side subjected to displacement and the resulting overall reaction force on the nodes located at the opposing fixed side were calculated. The response of the FE model for polycrystalline graphene was evaluated using average stress and strain values. The average strain in the x-direction, denoted as ϵ_x, is defined as the ratio of displacement along the loading direction to the side length of the FE model, and the average stress in this direction, represented as σ_x, is determined through dividing the total of reaction forces acting on all nodes located at the fixed side by the cross-sectional area of the sheet.

The suggested multiscale approach was employed to examine how the elastic properties of polycrystalline graphene are influenced by grain size. In this study, graphene sheets with varying average grain sizes and grain numbers, ranging from 12 to 1000 nm and from 25 to 200 grains were simulated. Some of these models are shown in Figure 3.6, as an example. Also, each simulation is repeated with random interactions for GBs. The elastic modulus corresponding to each grain size is determined as the averaged value of the FE simulations.

3.3 Results and discussion

3.3.1 Elastic properties of polycrystalline graphene from MD simulation

Defining elastic properties of polycrystalline graphene is achieved by conducting MD simulation on graphene sheets with dimensions of 20 $\times$ 20 nm and average grain sizes ranging from 2.7 to 10.3 nm. Displacement-controlled uniaxial tension deformation is applied in the y-direction by displacing the upper side of the sheet while keeping the lower side in a fixed position. Figure 3.7 represents snapshots

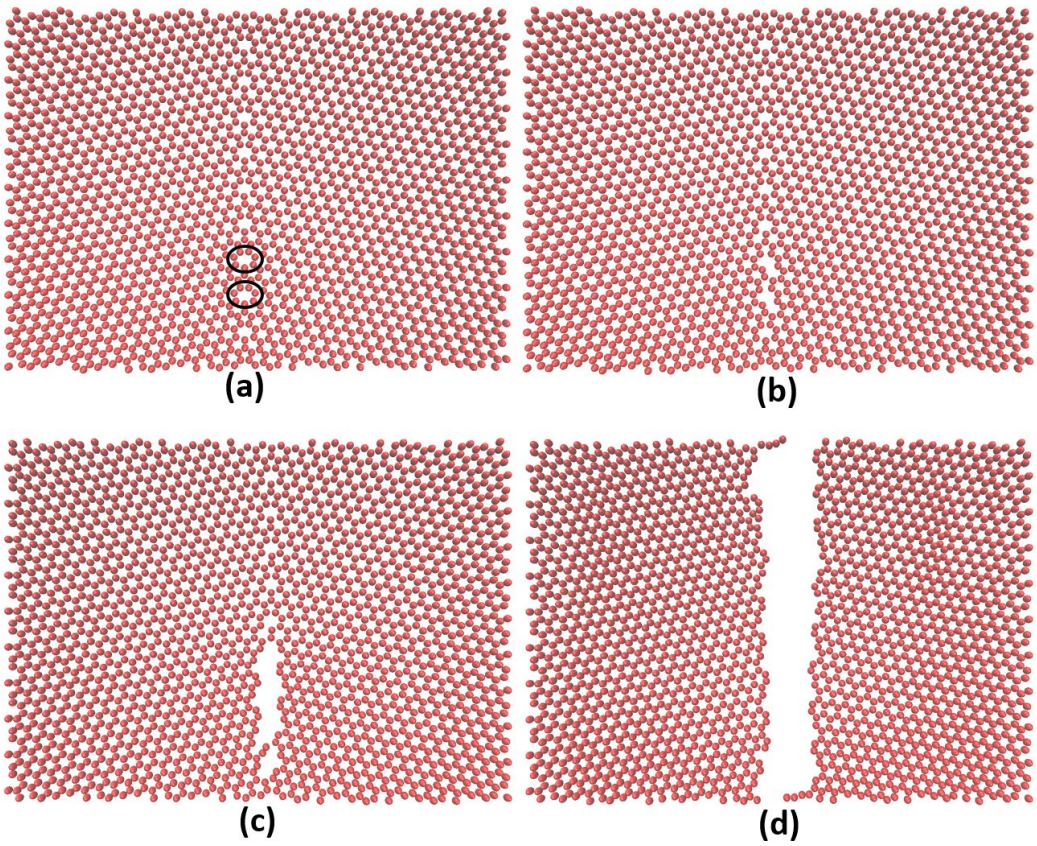

Figure 3.10: Different stages of the deformation in bicrystalline graphene sheet.

that correspond to different stages of the tensile loading. The crack initiation starts from a heptagon ring which is a stress concentration location (refer to Figure 3.7a). Subsequently, the crack propagates along the horizontal grain boundary, resulting in the complete fracture of the graphene sheet.

Figure 3.8 shows the stress-strain curves for the polycrystalline graphene sheets with different grain sizes. Additionally, the corresponding predicted Young's modulus (E) and fracture strength are presented in Figure 3.9. As expected, the grain size significantly influences both the elastic and fracture results.

3.3.2 Local properties of GBs for FE model

The local elastic properties of GBs (interphase regions) are defined through MD simulations performed on bicrystalline graphene sheets containing grain boundaries oriented in the y-direction, with misorientation angles ranging between 7.3 and 32.2

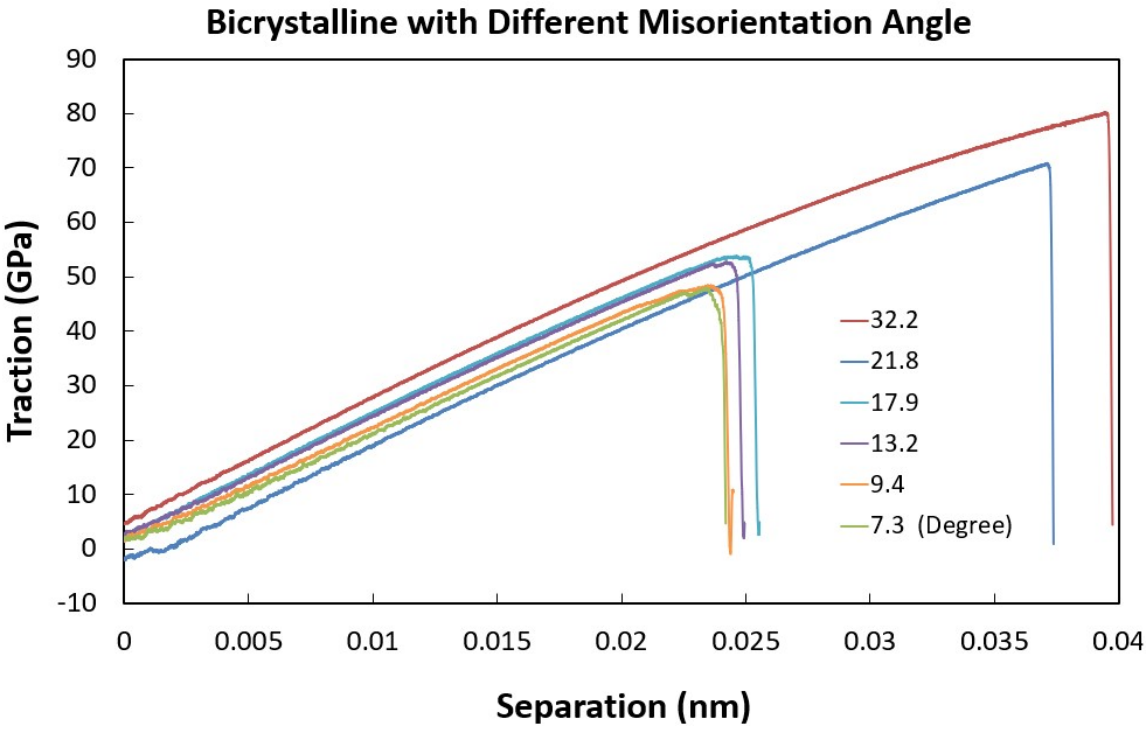

Figure 3.11: Stress-strain curves for bicrystalline graphene sheets with different misorientation angles.

degrees. Uniaxial tension deformation is applied by stretching the right side of the sheet in the x-direction, while the left side remains fixed. Figure 3.10 exhibits images capturing different stages of the deformation during the tensile loading. As evident from this figure, the crack formation begins from a pentagon ring, after which the crack propagates along the grain boundary leading to the complete rupture of the graphene sheet.

Stress-strain curves for bicrystalline graphene sheets featuring various misorientation angles are displayed in Figure 3.11. Moreover, corresponding cohesive zone parameters are provided in Figures 3.12-3.15. According to expectations, the lattice orientations of neighboring grains significantly impact the local elastic properties. The obtained elastic properties of the GBs are then applied to the developed a finite element model to determine the material properties of the polycrystalline graphene sheets on a larger scale.

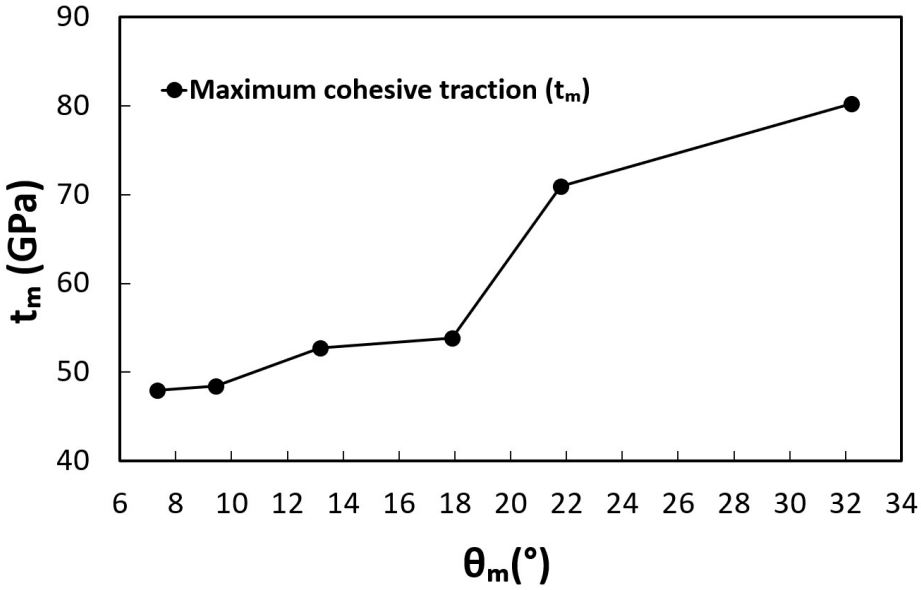

Figure 3.12: Maximum cohesive traction (t_m) versus GB misorientation angle.

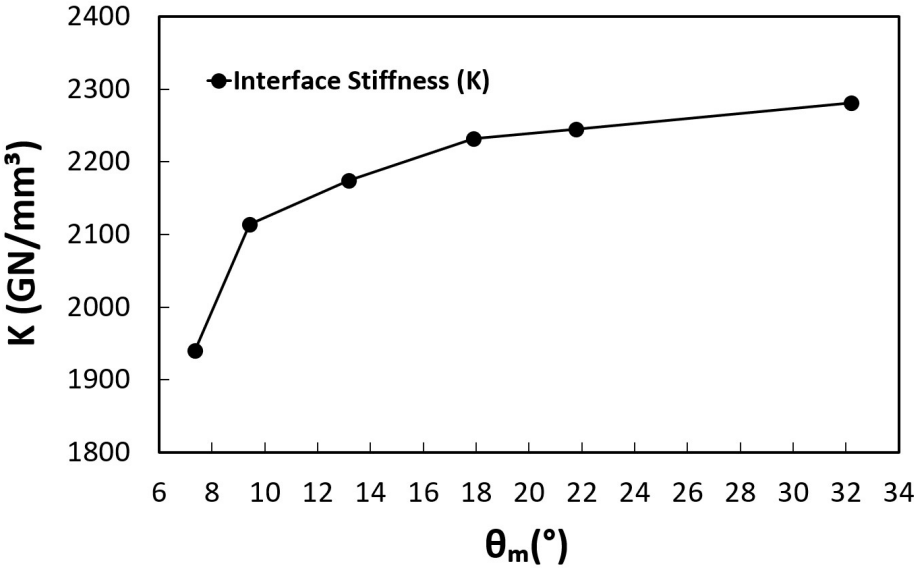

Figure 3.13: Interface stiffness versus GB misorientation angle.

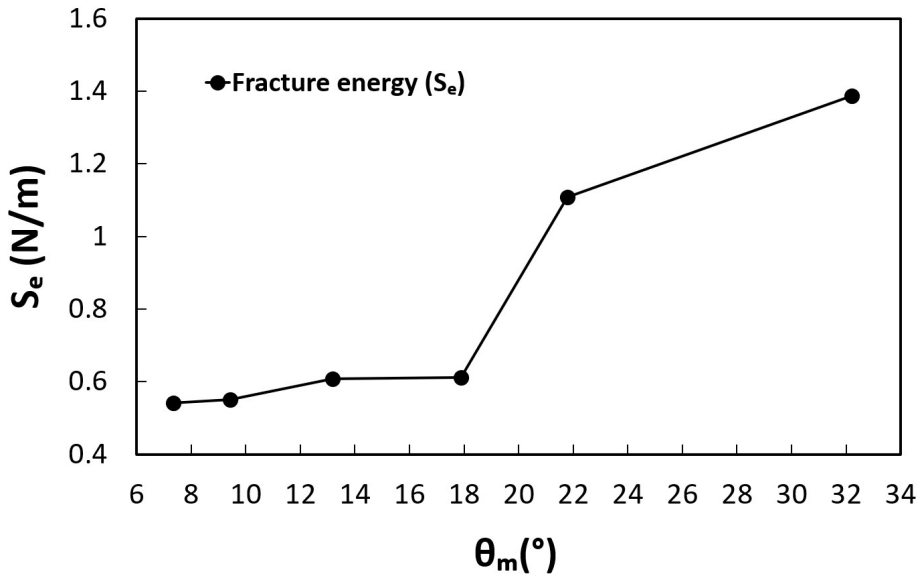

Figure 3.14: Work of separation (S_e) versus GB misorientation angle.

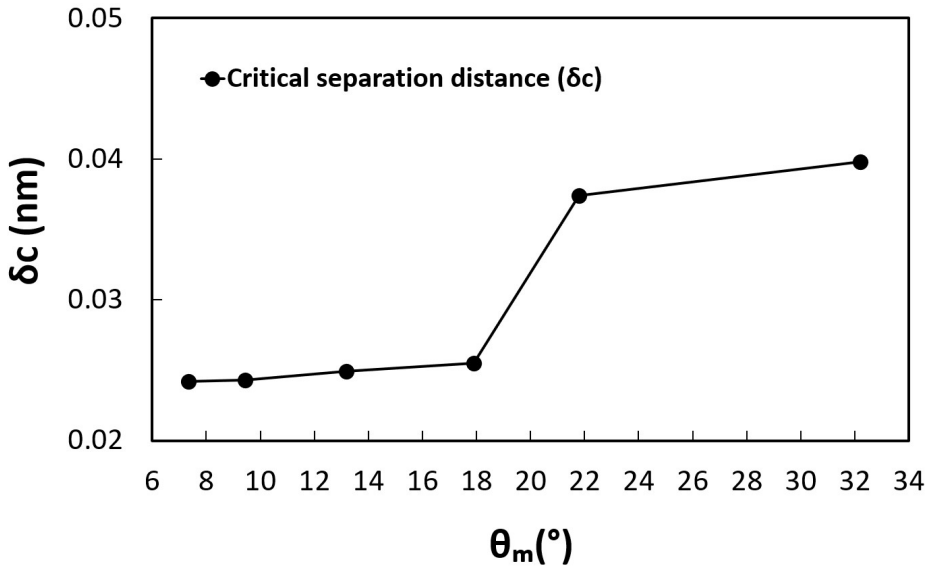

Figure 3.15: Critical separation distance (δ_c) versus GB misorientation angle.

3.3.3 Hybrid MD–FE multiscale simulations

Within this section, the results of the proposed hybrid model will be discussed. The elastic moduli of the pristine graphene and the local elastic properties of GBs derived through MD simulations are incorporated into the 2D plane stress FE model representing the material properties of the regions corresponding to the internal grains (E = 857 GPa) and interaction properties of the GBs, respectively. Similar to the MD simulations performed earlier, the system is subjected to uniaxial tensile deformation in the x-direction. The reaction forces on the fixed end of the FE model were monitored and recorded. Furthermore, the strain and stress contours, corresponding to both the loading direction and perpendicular to it, obtained from the finite element (FE) simulation, are displayed in Figure 3.16 and Figure 3.17, respectively. As anticipated from the boundary conditions, the stress and strain perpendicular to the loading direction are negligible. Additionally, as depicted in Figure 3.18, the stress and strain exhibit uniformity across different regions of the polycrystalline material (red points).

The maximum ϵ_x in the polycrystalline and pristine graphene are 2.561 and 1.522%, respectively. This implies that the polycrystalline graphene sheet is prone to failure under smaller deformation than the pristine graphene, because of the 68% increase in strain within the polycrystalline compared to the pristine graphene sheet.

3.3.4 Effect of grain size

The impact of grain size on the elastic properties of polycrystalline graphene was examined by employing a hybrid MD-FE multiscale modeling. In this study, MD and FE models were applied to study polycrystalline graphene sheets with average grain sizes varying from 2.7 to 10.3 nm and from 12 to 1000 nm, respectively. In Figure 3.19 and Figure 3.20, it can be observed that as the average grain size increases, the elastic modulus and fracture strength of the polycrystalline graphene sheets also experience

an increase. At the initial stage, there is a sharp increase in both the elastic modulus and fracture strength from 650 GPa to 839.07 GPa and from 44.5 GPa to 79.12 GPa, respectively, for sheets with average grain size ranging from 2.7 to 34 nm. These results suggest that in the cases with smaller grains, the influence of GBs predominates, resulting in reduced resistance to the applied loading. Subsequently, as the average grain size increased, the elastic modulus and fracture strength exhibited a gradual, continuous increase, eventually reaching 841.5 GPa and 79.16 GPa, respectively, for graphene sheets with an average grain size of 1000 nm. These values are 1.7% and 24% lower than the elastic modulus and fracture strength of pristine graphene derived through MD simulations, correspondingly. A summary of the results obtained through the MD and FE simulations is provided in Table 3.1.

Table 3.1: The elastic properties of the polycrystalline graphene derived from MD and FE simulations.

Type of Simulation	Grain Size (nm)	Young's modulus (GPa)	Fracture Stress (GPa)
Molecular Dynamics	2.7	650	44.5
	4.4	714	46.4
	6.2	730	47.9
	8.4	750	49.2
	10.3	782	50.6
Finite Element	12	817.62	53.05
	24	822.88	53.91
	34	839.07	79.12
	100	839.1	79.1235
	500	841.5317	79.1236
	750	841.5348	79.1601
	1000	841.5335	79.1623

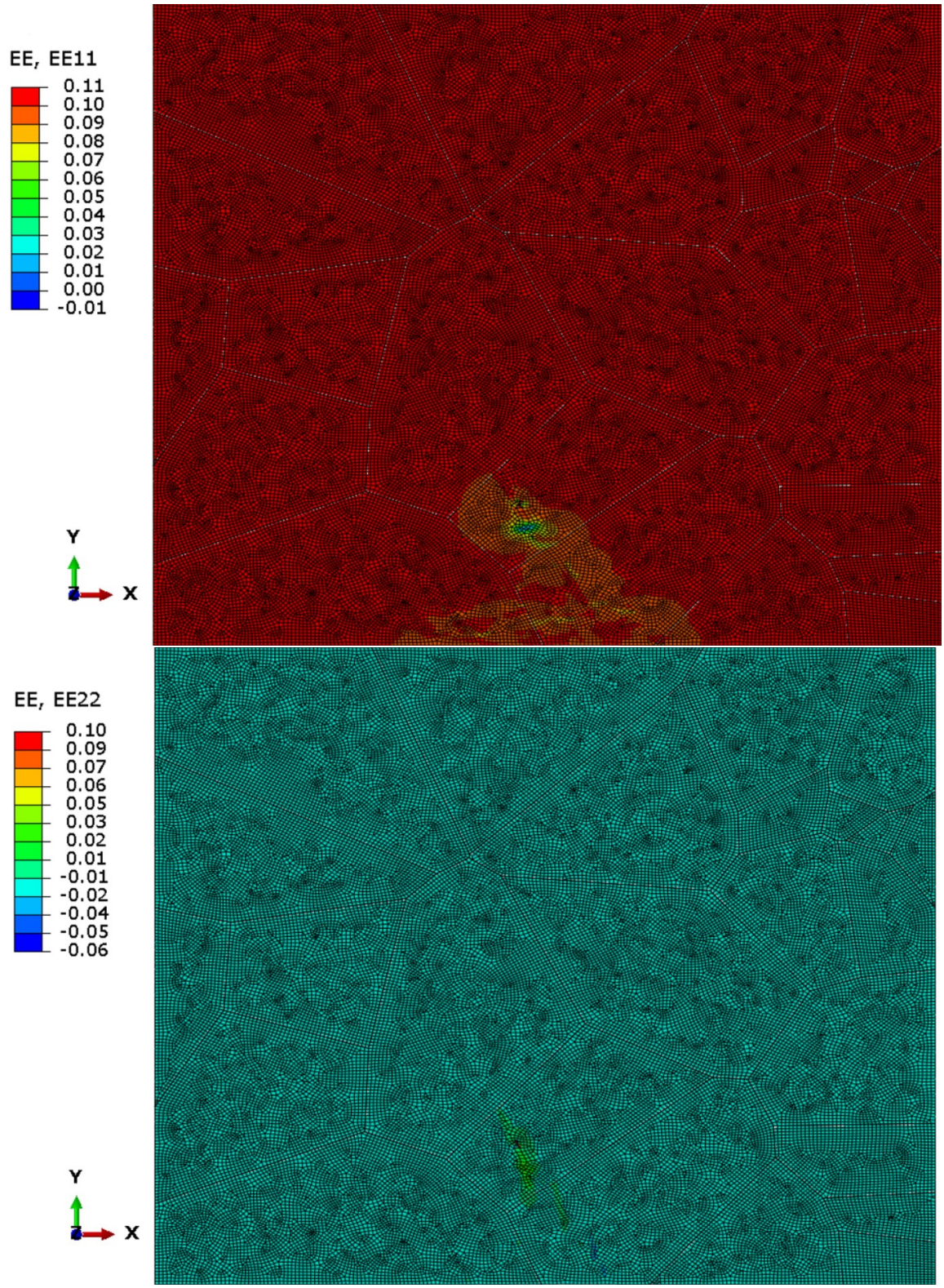

Figure 3.16: Comparison between strain contours aligned with and perpendicular to the loading direction.

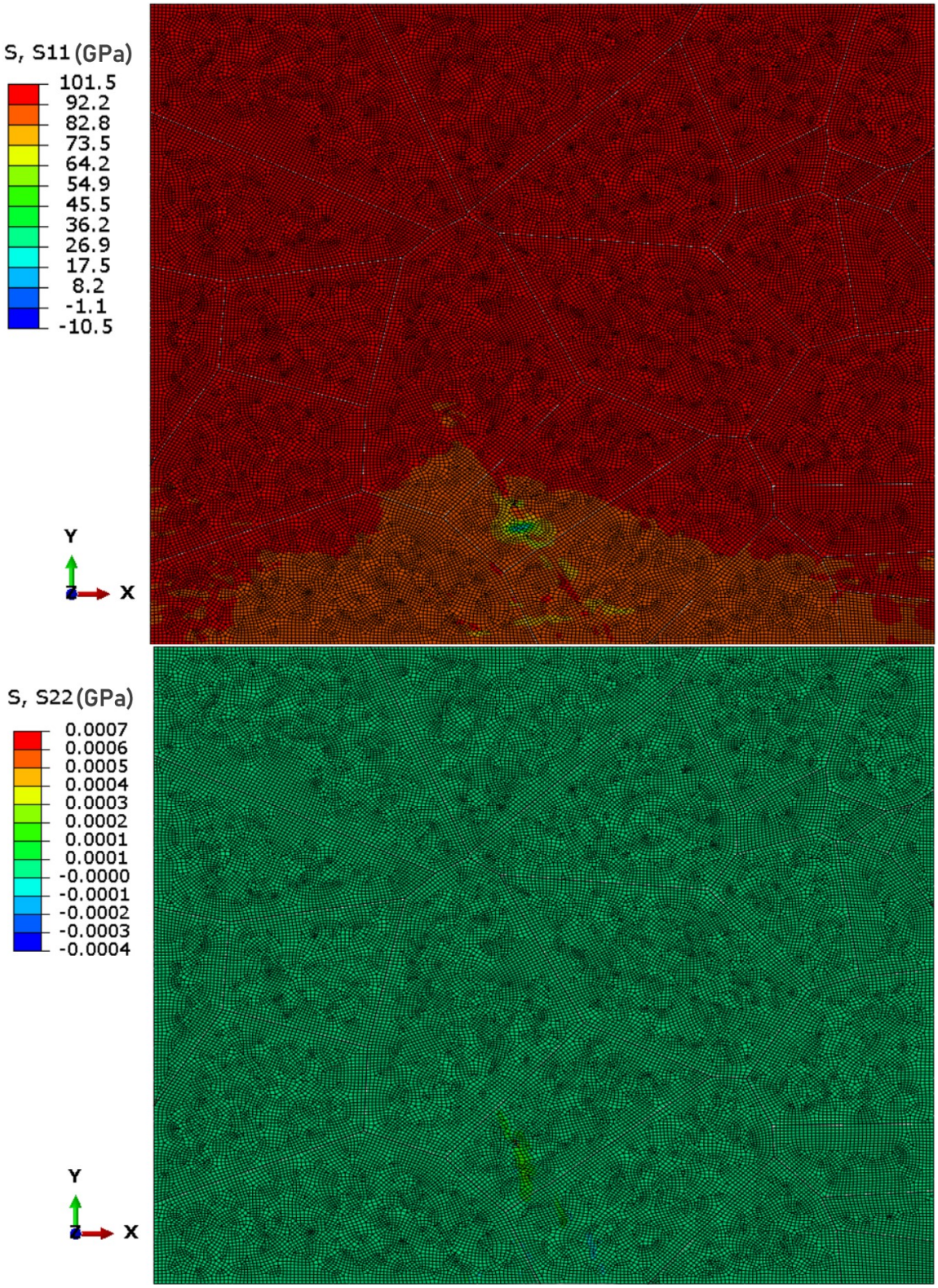

Figure 3.17: Comparison between stress contours aligned with and perpendicular to the loading direction.

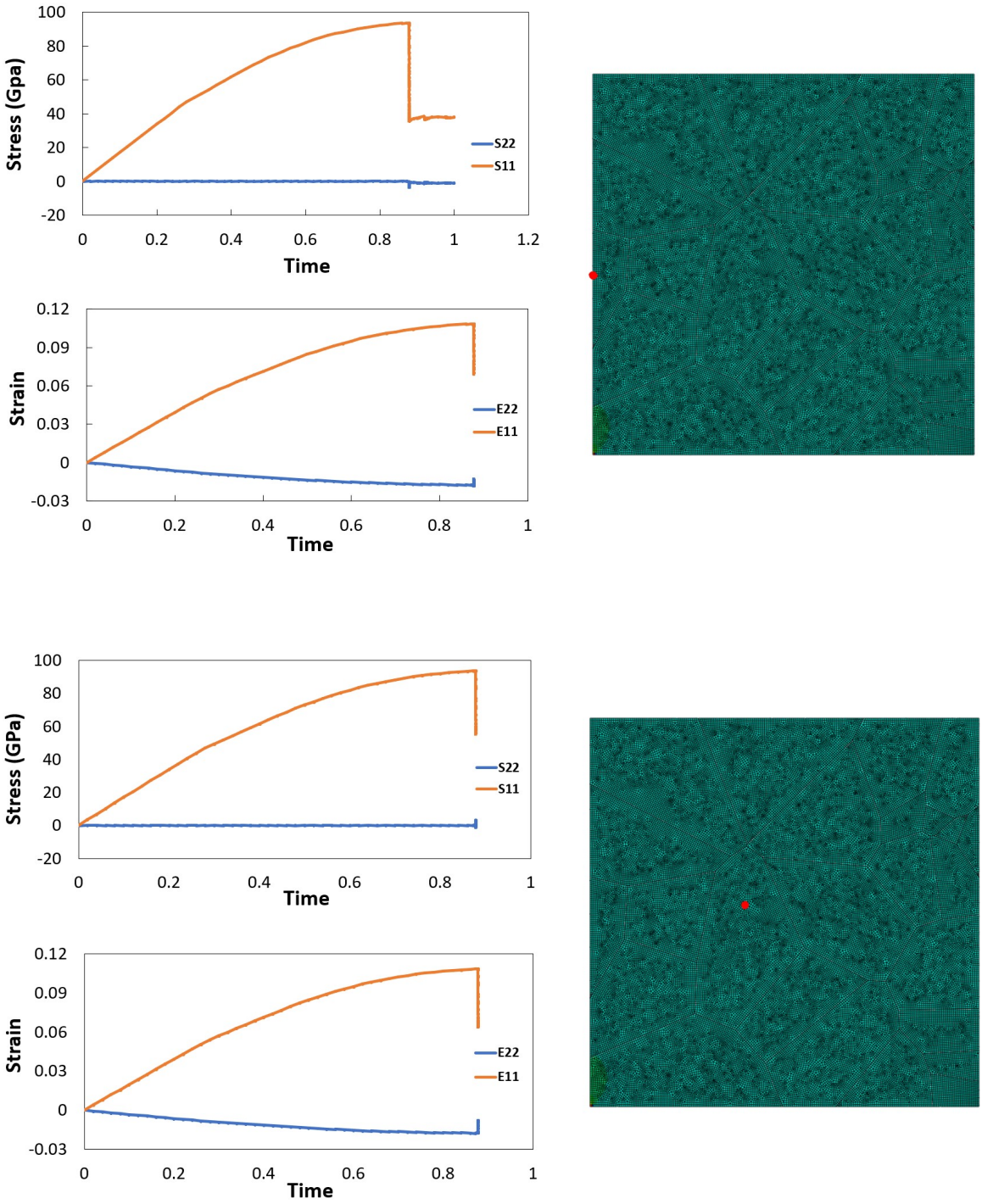

Figure 3.18: Comparison between stress and strain components across various regions of the polycrystalline.

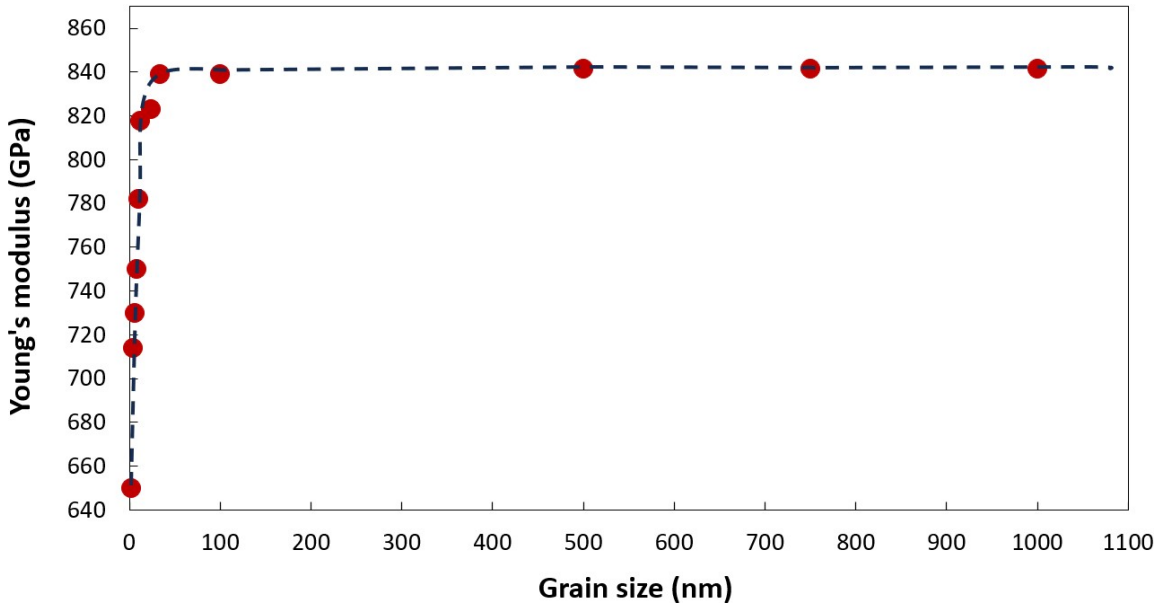

Figure 3.19: Correlations between the Young's modulus and the average grain size in polycrystalline graphene derived from both MD and FE simulations.

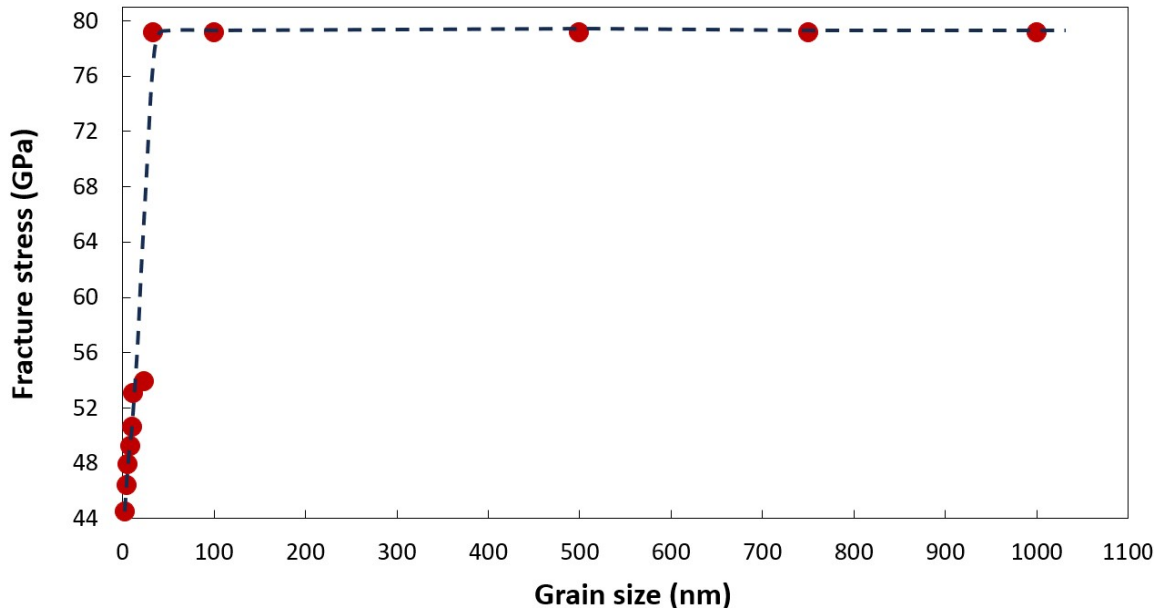

Figure 3.20: Correlations between the fracture stress and the average grain size in polycrystalline graphene derived from both MD and FE simulations.

3.4 Conclusions

In conclusion, this project investigates the mechanical properties of polycrystalline graphene across different scales, employing a multiscale molecular dynamics (MD)–finite element (FE) modeling approach. The research begins with MD simulations to study crack propagation and mechanical behavior at the nanoscale but utilizes FE analysis for modeling larger scale polycrystalline systems due to the limitations of atomic-level simulations. The study employs a novel multiscale methodology that combines the local properties extracted from MD simulations into FE simulations to examine the effect of grain size on mechanical properties such as Young's modulus and fracture stress.

The findings reveal a significant relationship between grain size and the mechanical properties of polycrystalline graphene. Smaller grain sizes are associated with reduced resistance to applied loading, primarily due to the influence of grain boundaries (GBs). As the average grain size increases, the elastic modulus and fracture strength of the polycrystalline graphene sheets gradually rise. These results have implications for industries interested in large scale polycrystalline graphene production, as understanding the impact of grain size is crucial for material design and applications.

This research represents a pioneering effort in the multiscale modeling of large scale polycrystalline graphene and contributes valuable insights into its mechanical behavior, which is essential for various industrial applications.

REFERENCES

[1] RJI Beatt, WL Birch, SE Hinton, M Kelly, MJ Pully, GRL Wright, and W Wright. Two-shift operation of 500 MW boiler/turbine generating units. *Proceedings of the Institution of Mechanical Engineers, Part A: Power and Process Engineering*, 197:247–255, 1983.

[2] Magdalena Speicher, Florian Kauffmann, Jae-Hyeok Shim, and Mahesh Chandran. Microstructure evolution in alloy 617 B after a long-term creep and thermal aging at 700 C. *Materials Science and Engineering: A*, 711:165–174, 2018.

[3] R Viswanathan and W Bakker. Materials for ultrasupercritical coal power plants—boiler materials: Part 1. *Journal of materials engineering and performance*, 10:81–95, 2001.

[4] JP Shingledecker, ND Evans, and GM Pharr. Influences of composition and grain size on creep–rupture behavior of inconel® alloy 740. *Materials Science and Engineering: A*, 578:277–286, 2013.

[5] F Sun, YF Gu, JB Yan, ZH Zhong, and M Yuyama. Phenomenological and microstructural analysis of intermediate temperatures creep in a Ni–Fe-based alloy for advanced ultra-supercritical fossil power plants. *Acta Materialia*, 102:70–78, 2016.

[6] Fazel Yavari and Nikhil Koratkar. Graphene-based chemical sensors. *The journal of physical chemistry letters*, 3:1746–1753, 2012.

[7] Dale AC Brownson, Dimitrios K Kampouris, and Craig E Banks. An overview

of graphene in energy production and storage applications. *Journal of Power Sources*, 196:4873–4885, 2011.

[8] Amartya Mukhopadhyay, Fei Guo, Anton Tokranov, Xingcheng Xiao, Robert H Hurt, and Brian W Sheldon. Engineering of graphene layer orientation to attain high rate capability and anisotropic properties in Li-Ion battery electrodes. *Advanced Functional Materials*, 23(19):2397–2404, 2013.

[9] Yi Han, Zhen Xu, and Chao Gao. Ultrathin graphene nanofiltration membrane for water purification. *Advanced Functional Materials*, 23(29):3693–3700, 2013.

[10] Jinhong Du and Hui-Ming Cheng. The fabrication, properties, and uses of graphene/polymer composites. *Macromolecular Chemistry and Physics*, 213(10-11):1060–1077, 2012.

[11] Xiao Huang, Xiaoying Qi, Freddy Boey, and Hua Zhang. Graphene-based composites. *Chemical Society Reviews*, 41(2):666–686, 2012.

[12] Yanwu Zhu, Hengxing Ji, Hui-Ming Cheng, and Rodney S Ruoff. Mass production and industrial applications of graphene materials. *National Science Review*, 5(1):90–101, 2018.

[13] EO Hall. The deformation and ageing of mild steel: III discussion of results. *Proceedings of the Physical Society. Section B*, 64(9):747, 1951.

[14] Gwan-Hyoung Lee, Ryan C Cooper, Sung Joo An, Sunwoo Lee, Arend Van Der Zande, Nicholas Petrone, Alexandra G Hammerberg, Changgu Lee, Bryan Crawford, Warren Oliver, et al. High-strength chemical-vapor–deposited graphene and grain boundaries. *science*, 340(6136):1073–1076, 2013.

[15] Yujie Wei, Jiangtao Wu, Hanqing Yin, Xinghua Shi, Ronggui Yang, and Mildred

Dresselhaus. The nature of strength enhancement and weakening by pentagon–heptagon defects in graphene. *Nature materials*, 11(9):759–763, 2012.

[16] Bohayra Mortazavi, Evgeny V Podryabinkin, Ivan S Novikov, Stephan Roche, Timon Rabczuk, Xiaoying Zhuang, and Alexander V Shapeev. Efficient machine-learning based interatomic potentials for exploring thermal conductivity in two-dimensional materials. *Journal of Physics: Materials*, 3(2):02LT02, 2020.

[17] Md Imrul Reza Shishir and Alireza Tabarraei. Traction–separation laws of graphene grain boundaries. *Physical Chemistry Chemical Physics*, 23(26):14284–14295, 2021.

[18] A Needleman. An analysis of tensile decohesion along an interface. *Journal of the Mechanics and Physics of Solids*, 38(3):289–324, 1990.

[19] Viggo Tvergaard and John W Hutchinson. The relation between crack growth resistance and fracture process parameters in elastic-plastic solids. *Journal of the Mechanics and Physics of Solids*, 40(6):1377–1397, 1992.

[20] Laurent Guin, Jean L Raphanel, and Jeffrey W Kysar. Atomistically derived cohesive zone model of intergranular fracture in polycrystalline graphene. *Journal of Applied Physics*, 119(24), 2016.

[21] Steven Cranford and Markus J Buehler. Twisted and coiled ultralong multilayer graphene ribbons. *Modelling and Simulation in Materials Science and Engineering*, 19(5):054003, 2011.

[22] John Frederick Nye. *Physical properties of crystals: their representation by tensors and matrices*. Oxford university press, 1985.

[23] Tianxiao Niu, Guoxin Cao, and Chunyang Xiong. Fracture behavior of graphene mounted on stretchable substrate. *Carbon*, 109:852–859, 2016.

CHAPTER 4: Fracture Mechanics of Tetragraphene Under Mixed Mode Loading

4.1 Introduction

The need to overcome the limitations of graphene in electronic applications has prompted numerous investigations into the exploration of novel two-dimensional carbon-based materials that could potentially introduce an electronic bandgap. Graphene has many 2D carbon allotropes; a quasi-2D semiconductor carbon allotrope, called tetragraphene (TG), was recently proposed. TG is composed of hexagonal and tetragonal rings and shows metallic or semiconducting behaviors with no limitations in electronic applications. This study uses molecular dynamics (MD) simulations to understand fracture properties of triple-layered TG sheets with two different atomic structures under mixed mode I and II loading using the Tersoff–Erhart potential. We investigate the effect of loading phase angle, crack edge chirality, crack tip configuration, and temperature on the crack propagation path and critical stress intensity factors in two different TG structures. The findings reveal that the critical stress intensity factor and crack propagation path are influenced by all of these factors, except for cases where the loading phase angle is 0°.

Over the last few years, nanomaterials have revolutionized the landscape of materials science and engineering [1, 2, 3, 4, 5, 6, 7], providing a platform for the development of groundbreaking technologies with unmatched properties. Among these fascinating nanomaterials, tetragraphene (TG) stands out as a two-dimensional carbon allotrope that demonstrates extraordinary characteristics and structural stability. In contrast to graphene, which is a semimetal and suffers from the lack of an intrinsic band gap [8, 9], limiting its direct application in electronic devices, tetragraphene possesses a unique lattice structure that offers exciting opportunities for tailoring its electronic

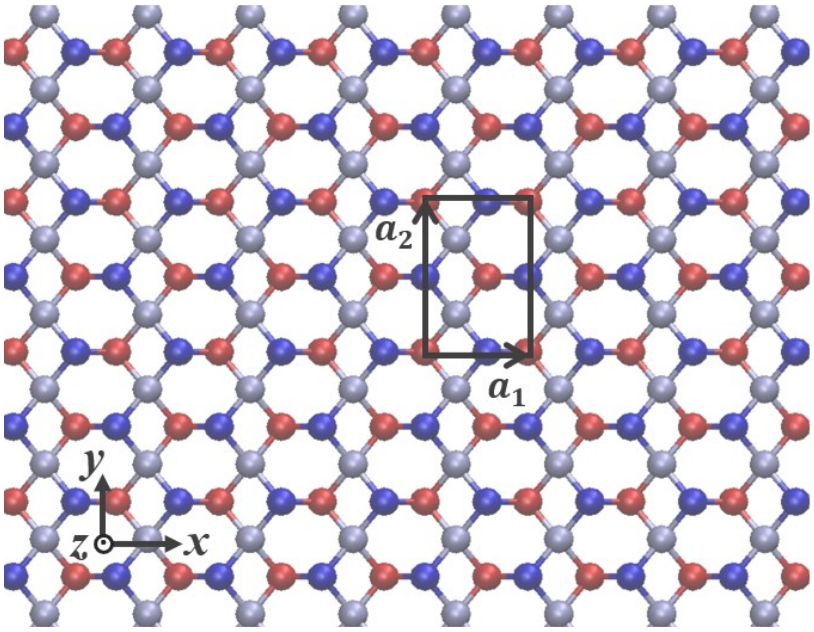

(a)

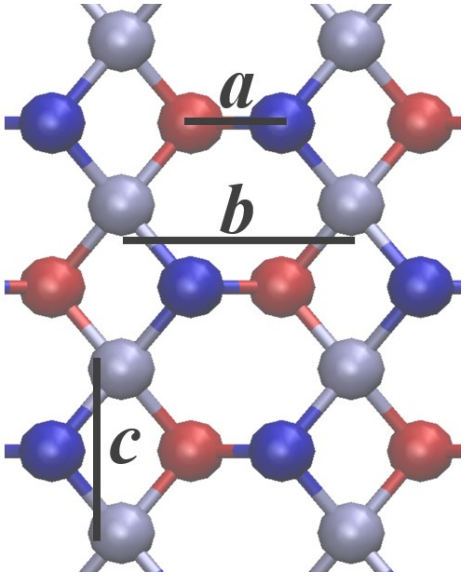

(b)

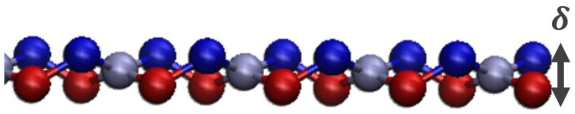

(c)

Figure 4.1: 2-Even Tetragraphene structure from (a), (b) top, and (c) side views. δ, a, b, and c represent TG's thickness, the distance between two tri-coordinated, tetra-coordinated atoms, and the diagonal length of the tetragonal rings, respectively. The upper-layer (lower-layer) tri-coordinated atoms and the central-layer tetra-coordinated atoms are in blue (red) and gray colors.

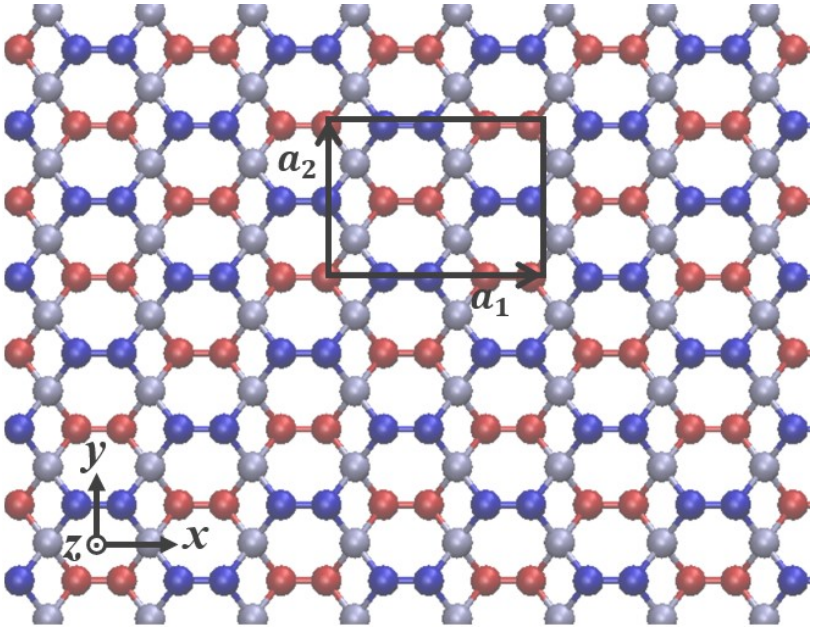

(a)

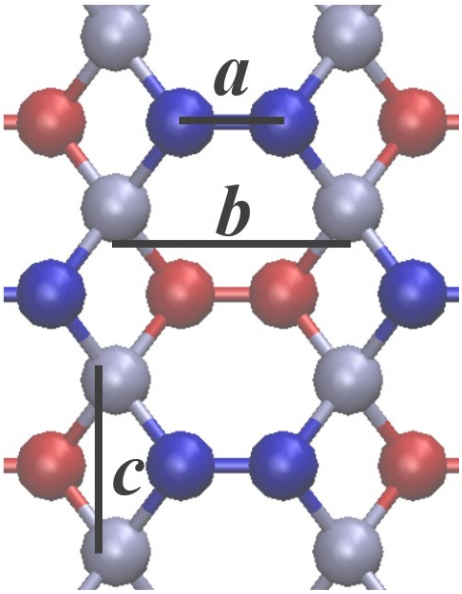

(b)

Figure 4.2: 2-Odd tetragraphene structure from the top view. a, b, and c represent the distance between two tri-coordinated, tetra-coordinated atoms and the diagonal length of the tetragonal rings, respectively. The upper-layer (lower-layer) tri-coordinated atoms and the central-layer tetra-coordinated atoms are in blue (red) and gray colors.

band structure [10]. This property opens new vistas for employing tetragraphene in electronic applications, potentially overcoming one of the major challenges faced by graphene-based devices. Moreover, the fourfold symmetry of tetragraphene introduces electronic anisotropy, signifying that its electronic properties may vary significantly with direction . This intriguing characteristic can be ingeniously harnessed in designing novel electronic devices with tailored functionalities and precise electronic behavior, adding an extra layer of versatility to the material's potential applications.

While graphene's mechanical and fracture properties have been extensively studied [11, 12, 13, 14, 15], more investigation is needed to comprehend the fracture characteristics of other graphene-like two-dimensional materials such as TG. Unlike graphene's flat structure, TG's atomic structure is more intricate, with a triple-layered arrangement in each sheet. Consequently, TG's failure mechanisms are more complex than those of graphene. As a result, a distinct analysis of TG's fracture properties is essential, as they may vary significantly from those of graphene.

Given the challenges in conducting experiments at the nanoscale, computational methods such as molecular dynamics and density functional theory have become invaluable in studying the properties of two–dimensional materials. Brandao et al. [16] utilized molecular dynamic simulations to evaluate the mechanical properties of tetragraphene. Their simulations indicated a transition from a crystalline to an amorphous structure induced by applying temperature and/or tension. De Vasconcelos et al. [17] studied the stability, as well as the electronic and magnetic properties of tetragraphene nanoribbons, by using first-principles calculations based on the density functional theory (DFT). They examined how the electronic properties of these nanoribbons depend on their width, chirality, and edge atom reconstruction. De Vasconcelos et al. [18] analyzed the electronic properties of tetragraphene using the DFT method, and they determined that it shows metallic or semiconducting behaviors, depending on its structural parameters. Furthermore, it has been noticed that

TG has high electronic mobility with smaller cohesion energy than penta-graphene. Hence, TG could be a good choice for high-performance electronic devices [19]. Wei et al. [10] explored how TG behaves under uniaxial tensile strain and found that it has superior ultrahigh strength and ductility by using DFT calculations. Kilic and Lee [20] utilized DFT calculations to examine the stability, structural, mechanical, thermal, electronic, and optical properties of TG and its hydrogenated derivatives. Based on their findings, there is a decrease in thermal conductivity and an increase in specific heat capacity in hydrogenated derivatives of TG. Moreover, they found that hydrogenation reduces in-plane stiffness and Young's modulus, but increases ultimate strength. In another study conducted by Kilic and Lee [21], the stability of TG and its fluorinated derivatives is investigated from different aspects such as energetic, dynamic, thermal, and mechanical through DFT calculations.

This research aims to explore the fracture properties of TG through molecular dynamic simulations, with a specific focus on examining the crack propagation path and critical stress intensity factors under mixed mode I and II loading conditions.

4.2 Structure of Tetragraphene

The atomic structures of TG studied in this work are shown in Figure 4.1 and Figure 4.2. It consists of three layers, with a middle layer comprising tetra-coordinated carbon atoms connected by two sandwiching layers of tri-coordinated carbon atoms. The upper-layer tri-coordinated atoms are marked in blue, while the lower-layer ones are shown in red. The central-layer tetra-coordinated atoms are displayed in gray. Figure 4.1b and Figure 4.2b illustrate the geometric parameters a, b, and c. These parameters respectively represent the distance between two tri-coordinated neighbors, the distance between two tetra-coordinated atoms in the a_1 direction, and the diagonal length of the tetragonal rings along the a_2 direction. Additionally, Figure 4.1c depicts the layer thickness.

The unit cells of TG-2-even and TG-2-odd structures are shown in Figure 4.1a and

Figure 4.2a, respectively. They are rectangular consisting of 6 and 12 carbon atoms for 2-even and 2-odd cases, respectively. The corresponding lattice vectors for these cells are:

$$a_1 = (a_x, 0) \qquad a_2 = (0, a_y) \tag{4.1}$$

The structures shown in Figure 4.1 and Figure 4.2 will be referred to as TG-2-even and TG-2-odd, respectively. The name even or odd is derived from the observation that successive tri-coordinated atoms in a direction perpendicular to the tetragons lines (do not) swap layers for the (even) odd case. Moreover, the reason for the index 2 comes from the fact that between the lines of tetragonal rings, there are two lines of hexagons which can be seen as two neighboring zigzag strips of atoms.

4.3 Computational Method

We use molecular dynamics (MD) simulations to study the stress intensity factor and crack propagation path of triple-layered tetragraphene under mixed mode I (opening mode) and mode II (in-plane shear mode) loading. The LAMMPS package is utilized to perform the molecular dynamics simulations [22]. Interactions between carbon atoms in the TG sheets are modeled using the Tersoff Erhart-Albe potential [23]. Our MD model is a circular domain cut around the crack tip as shown in Figure 4.2. The domain is selected large enough to ensure that its boundary is located within the K-dominant zone. To obtain the equilibrium configuration of the cracked domain, first, the crack tip asymptotic field is applied to all the atoms in the domain, and then while the interior atoms are in a relaxed position, the boundary atoms are held fixed. The crack tip asymptotic displacement fields for a linear isotropic material can be written as [24]:

$$u_x = \frac{1+\nu}{E}\sqrt{\frac{r}{2\pi}}\Bigg[K_I \cos\frac{\theta}{2}\left(\kappa - 1 + 2\sin^2\frac{\theta}{2}\right) + K_{II}\sin\frac{\theta}{2}\left(\kappa + 1 + 2\cos^2\frac{\theta}{2}\right)\Bigg]$$

$$u_y = \frac{1+\nu}{E}\sqrt{\frac{r}{2\pi}}\Bigg[K_I \sin\frac{\theta}{2}\left(\kappa + 1 - 2\cos^2\frac{\theta}{2}\right) - K_{II}\cos\frac{\theta}{2}\left(\kappa - 1 - 2\sin^2\frac{\theta}{2}\right)\Bigg] \tag{4.2}$$

where u_x and u_y respectively represent the displacement components in the x and y directions, K_I and K_{II} denote mode I and mode II stress intensity factors, r and θ are the polar coordinates shown in Figure 4.3.

E and ν denote Young's modulus and Poisson's ratio of the TG sheet, respectively. To define their values, a uniaxial tensile deformation is applied in the x and y directions. From the corresponding stress-strain curves, shown in Figure 4.4, the final values of Young's modulus and Poisson's ratio are determined based on the average value, which are $E = 583$ GPa, $\nu = 0.2$ and $E = 627$ GPa, $\nu = 0.2$ for 2-even and 2-odd structures, respectively.

The Kolosov constant, represented by κ, can be expressed as $\frac{3-\nu}{1+\nu}$ for plane stress conditions. The effective stress intensity factor is expressed by $K_{eff} = \sqrt{K_I^2 + K_{II}^2}$, and the loading phase angle is determined as $\phi = \tan^{-1}(\frac{K_{II}}{K_I})$, which demonstrates the ratio of the mode I and mode II loading. According to this definition, a loading phase angle of 0° indicates pure mode I loading, while a loading phase angle of 90° corresponds to pure mode II loading. In this study, the loading phase angle is changed from 0° to 90° to analyze its effect on the critical stress intensity factor, K_{cr}.

To model crack propagation under quasi-static loading, the loading is increased in increments of $\Delta K_{eff} = 0.01\text{MPa}\sqrt{\text{m}}$. Following each loading increment, the

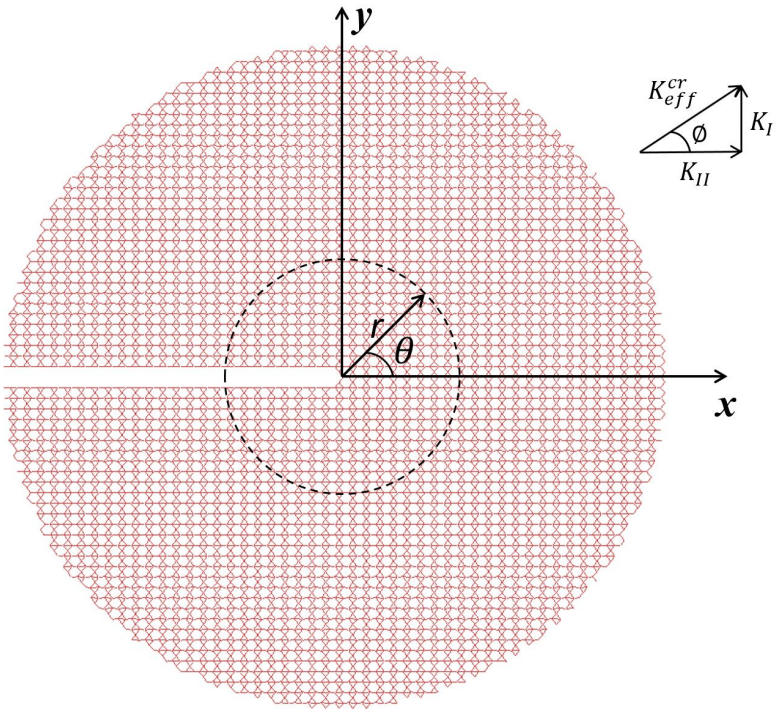

Figure 4.3: Molecular dynamic domain

positions of boundary atoms are kept fixed, while the positions of interior atoms are relaxed using the conjugate gradient method. The velocity-rescaled Berendsen thermostat is used to increase the temperature of the interior domain to the desired value. After a relaxation period of 3 ps in a microcanonical (NVE) ensemble, a Nosé-Hoover thermostat is applied to maintain the temperature at the specified value for 60 ps within a canonical (NVT) ensemble. The velocity-Verlet algorithm with a time step of 1 fs is utilized to integrate the atoms' trajectory over time. This simulation process is repeated for various temperatures ranging from 0 K to 2000 K at each loading phase angle to investigate the effect of temperature on TG's fracture properties. In this research, the stress intensity factor at which the first bond at the crack tip or crack edge breaks is referred to as the critical stress intensity factor. The covalent bond length of the atoms located at the crack tip and crack edge is checked after each load increment; if the length exceeds the potential cutoff distance, the bond is considered broken.

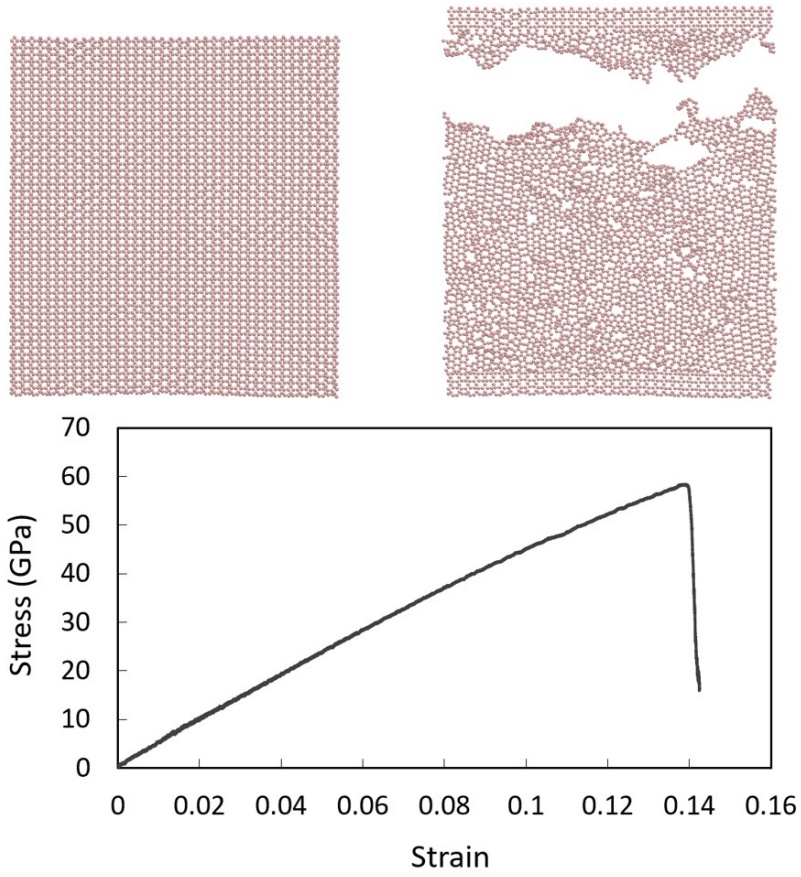

Figure 4.4: Tensile loading on TG sheet.

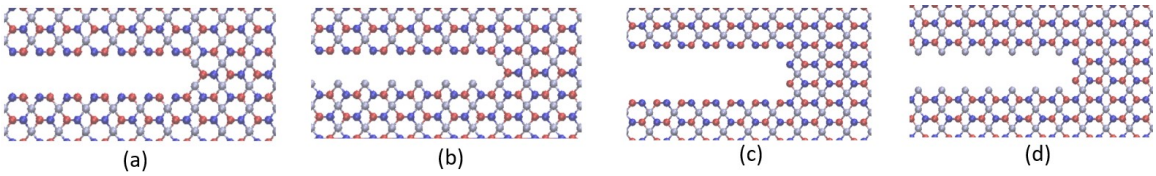

Figure 4.5: Schematic of the 4 crack types for 2-even structure: (a) ZZ sharp crack, (b) Asymmetric(ZZ/AC) sharp crack, and c) ZZ blunt crack (d) AC blunt crack.

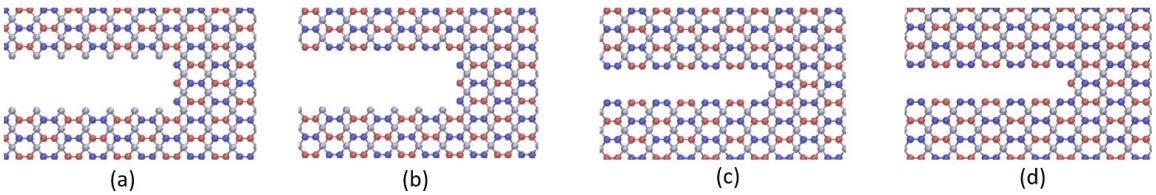

Figure 4.6: Schematic of the 4 crack types for 2-odd structure: (a) AC blunt crack, (b) Asymmetric(ZZ/AC) blunt crack, and c) ZZ sharp crack (d) ZZ blunt crack.

The effect of crack edge chirality on fracture properties is investigated by considering zigzag (ZZ) and armchair (AC) cracks, which have symmetrical edges. Additionally, the cracks with asymmetric edges, where one edge has ZZ chirality and the other AC chirality, are studied for comparison with the symmetric case. Moreover, to explore crack tip configuration impact on the critical stress intensity factors and crack propagation paths sharp (Figures 4.5a and b) and blunt (Figures 4.5c and d) shapes are considered for the crack tip. Figures 4.5 and 4.6 represent different crack structures studied in this project for 2-even and 2-odd cases respectively.

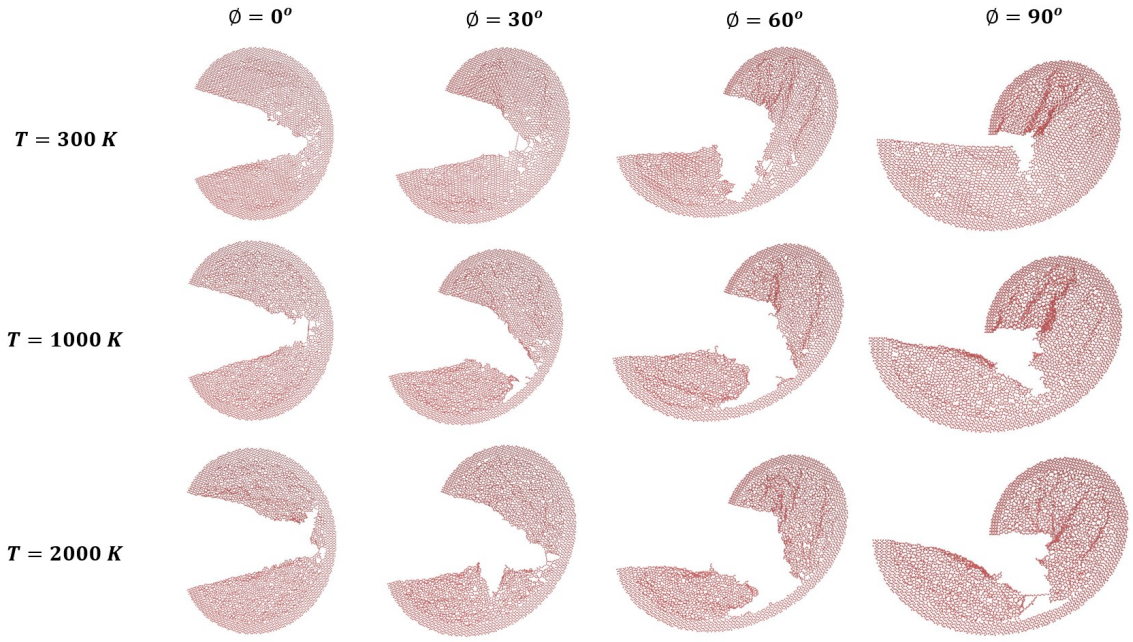

Figure 4.7: Crack propagation paths in a 2-even TG sheet including a sharp symmetric(ZZ) crack.

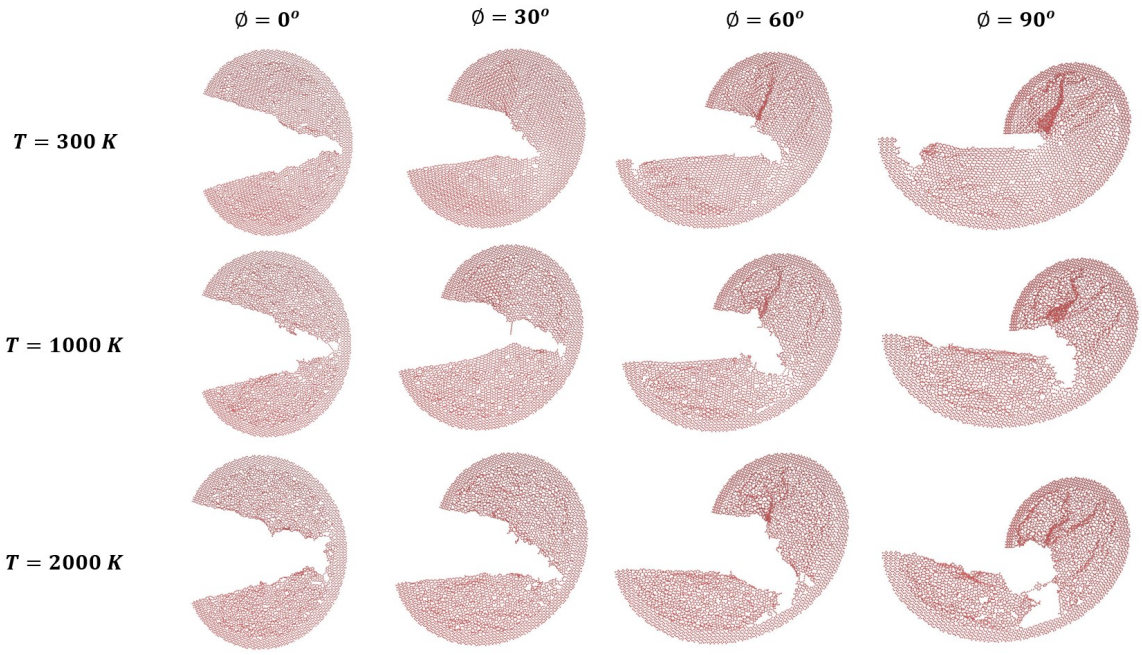

Figure 4.8: Crack propagation paths in a 2-even TG sheet including a sharp asymmetric(ZZ-AC) crack.

4.4 Results and Discussion

The crack propagation paths in TG-2-even and TG-2-odd structures including different crack structures are displayed in Figures 4.7-4.12. The results demonstrate that the loading phase angle and temperature affect the crack propagation path. Moreover, Figures 4.11 and 4.12 illustrate that in addition to loading phase angle and temperature, the crack propagation path is influenced by crack edge chirality and crack tip configuration. It could be observed from the plots that for loading phase angles greater than zero, the cracks can kink as they continue to grow, and there is little to no out-of-plane deformation when the loading phase angle is close to zero. However, as the loading phase angle approaches 90°, the out-of-plane deformation becomes more pronounced. This indicates that the out-of-plane deformation is significant when mode II loading dominates. The out-of-plane deformation under pure mode II loading is shown in Figures 4.13 and 4.14. Indeed, buckling of the TG sheet under compressive loading causes out-of-plane deformation, which results in

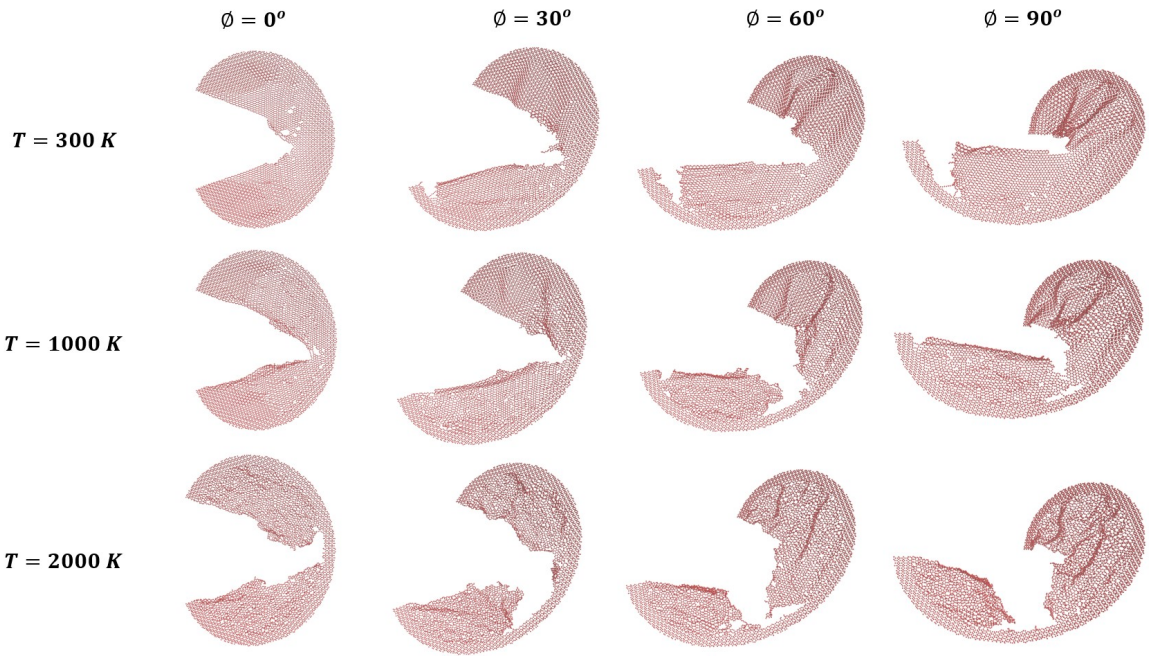

Figure 4.9: Crack propagation paths in a 2-odd TG sheet including a blunt symmetric(AC) crack.

energy release through bending and can delay crack propagation. This phenomenon has been previously reported in pre-cracked thin plates under tensile or shear loading [25]. It is anticipated to occur in some other two-dimensional materials, such as TG. Also, under a loading phase angle equal to zero (pure mode I loading), the crack will propagate along a self-similar path.

The correlation between the effective critical stress intensity factor and temperature, crack tip configuration, and crack edge chirality is illustrated through Figures 4.15-4.21. As it is clear from Figures 4.15 and 4.16, an increase in temperature leads to a decrease in stress intensity factor for both 2-even and 2-odd structures. The plots of Figure 4.17 show how crack tip configuration affects the stress intensity factor. The mode I stress intensity factor is nearly identical for both sharp and blunt configurations. For a loading phase angle less than about 40°, the critical stress intensity factor is larger for the blunt crack tip, and when the loading phase angle is larger than 40°, a sharp crack tip has a higher critical stress intensity factor. Moreover,

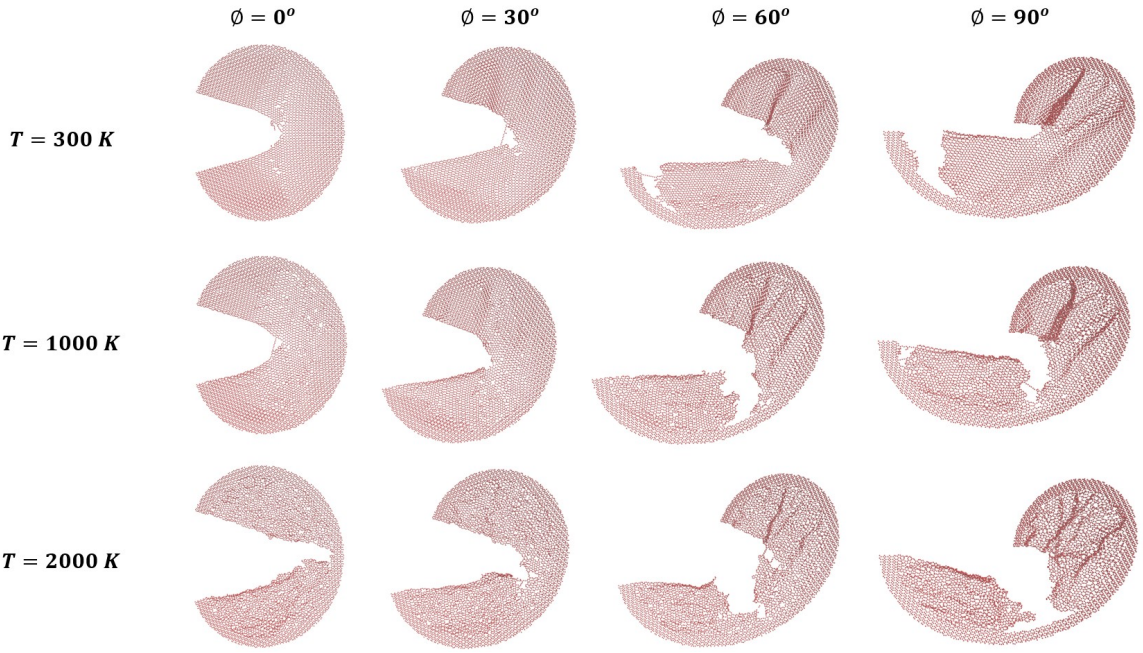

Figure 4.10: Crack propagation paths in a 2-odd TG sheet including a blunt asymmetric(ZZ-AC) crack.

the results presented in Figure 4.18 indicate that zigzag cracks have a higher critical stress intensity factor compared with armchair cracks. Interestingly, once more, the mode I stress intensity factor is almost the same for zigzag and armchair cracks. Additionally, Figures 4.19 and 4.20 compare symmetric and asymmetric cracks in terms of critical stress intensity factor for 2-odd and 2-even structures, respectively. It could be concluded that asymmetric cracks have a higher stress intensity factor except for mode I which is almost the same for both symmetric and asymmetric cracks. Lastly, a comparison of TG-2-even and TG-2-odd structures reveals that the 2-odd structure has a higher critical stress intensity factor, Figure 4.21. In general, the results show a higher critical stress intensity factor for pure mode II compared to mode I. This suggests that the propagation of cracks under a shearing mode necessitates more energy compared to the energy needed for crack propagation under an opening mode. This is attributed to the generation of out-of-plane deformation when mode II is prevalent. A portion of the applied loading energy is used through the elastic energy associated

with buckling bending, requiring additional external energy for breaking the bond at the crack tip or crack edge. Also, the increase in the critical stress intensity factor which occurs as the loading phase angle approaches 90° is related to this phenomenon.

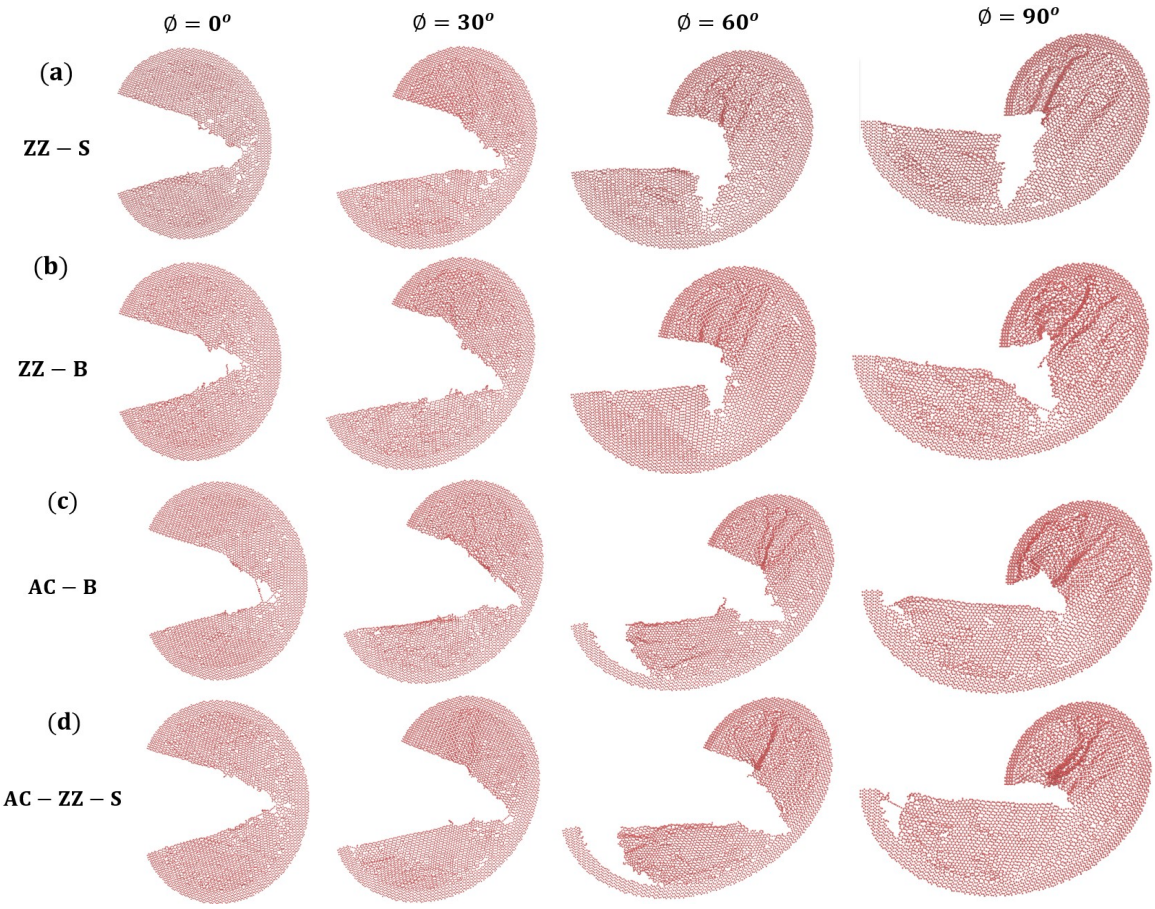

Figure 4.11: Crack propagation paths in a 2-even TG sheet. (a) Sharp ZZ crack, (b) Blunt ZZ crack, (c) Blunt AC crack, (d) Sharp AC-ZZ crack.

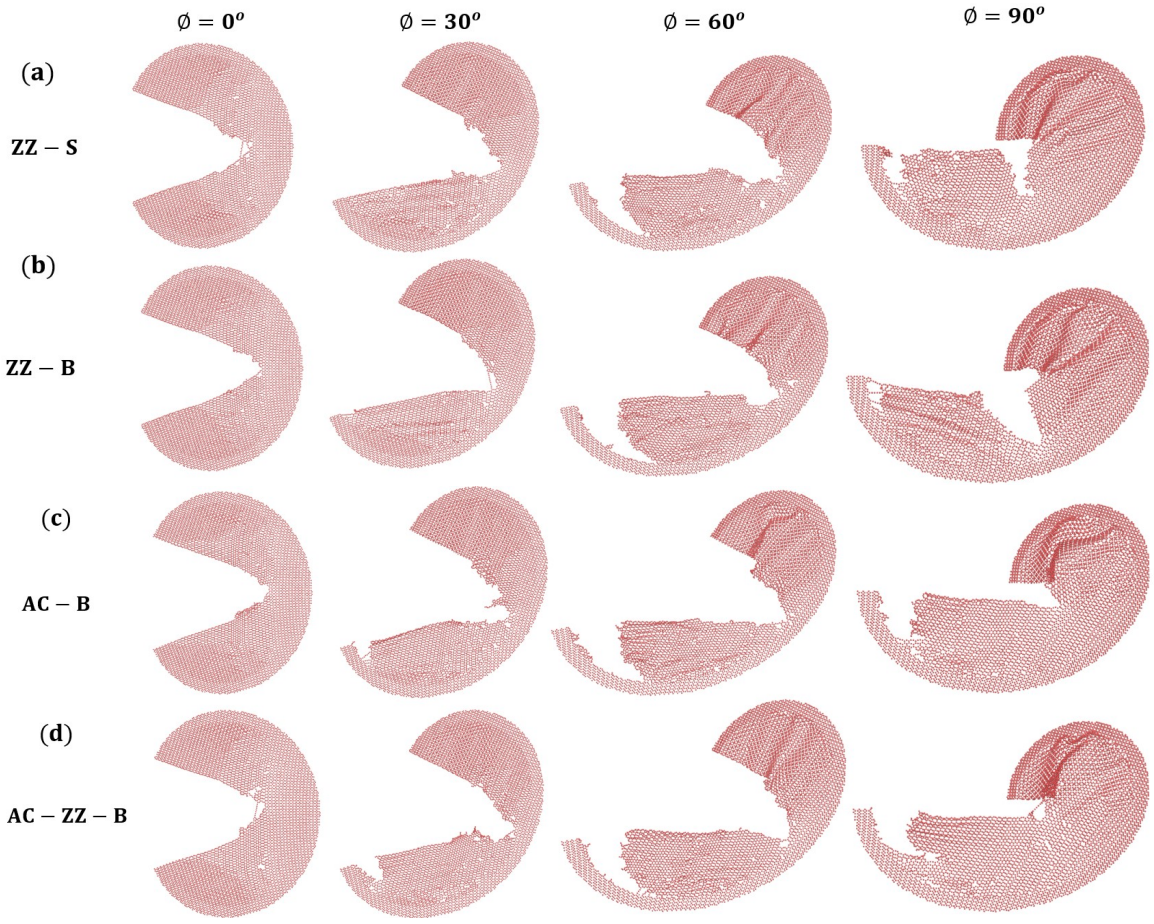

Figure 4.12: Crack propagation paths in a 2-odd TG sheet. (a) Sharp ZZ crack, (b) Blunt ZZ crack, (c) Blunt AC crack, (d) Blunt AC-ZZ crack.

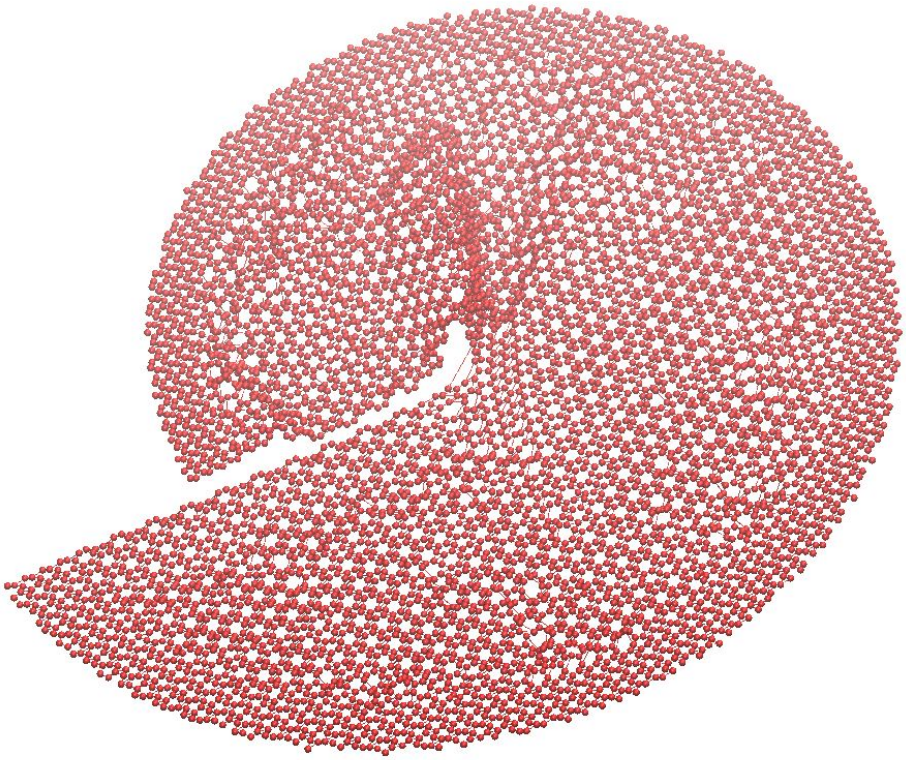

Figure 4.13: Buckling under pure mode II loading

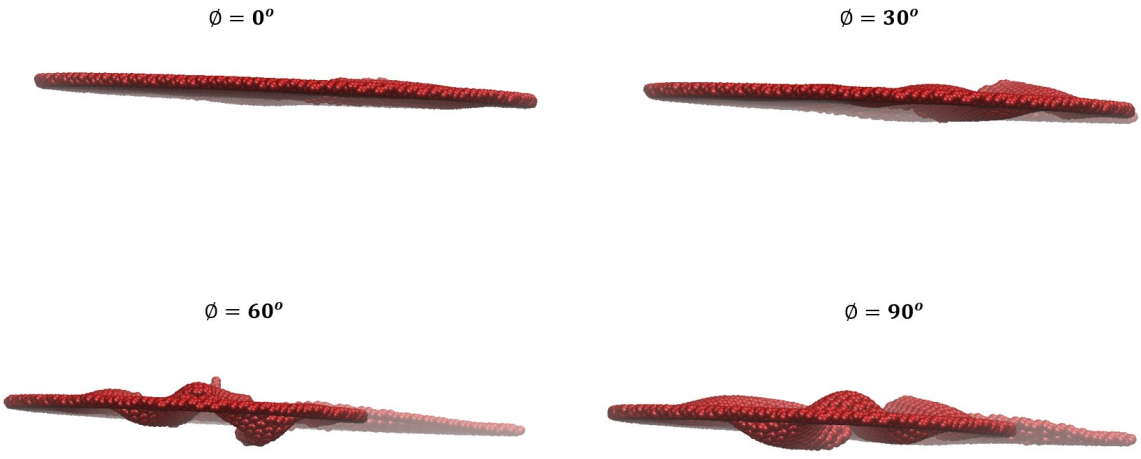

Figure 4.14: Out-of-plane deformation of the TG sheet from the side view.

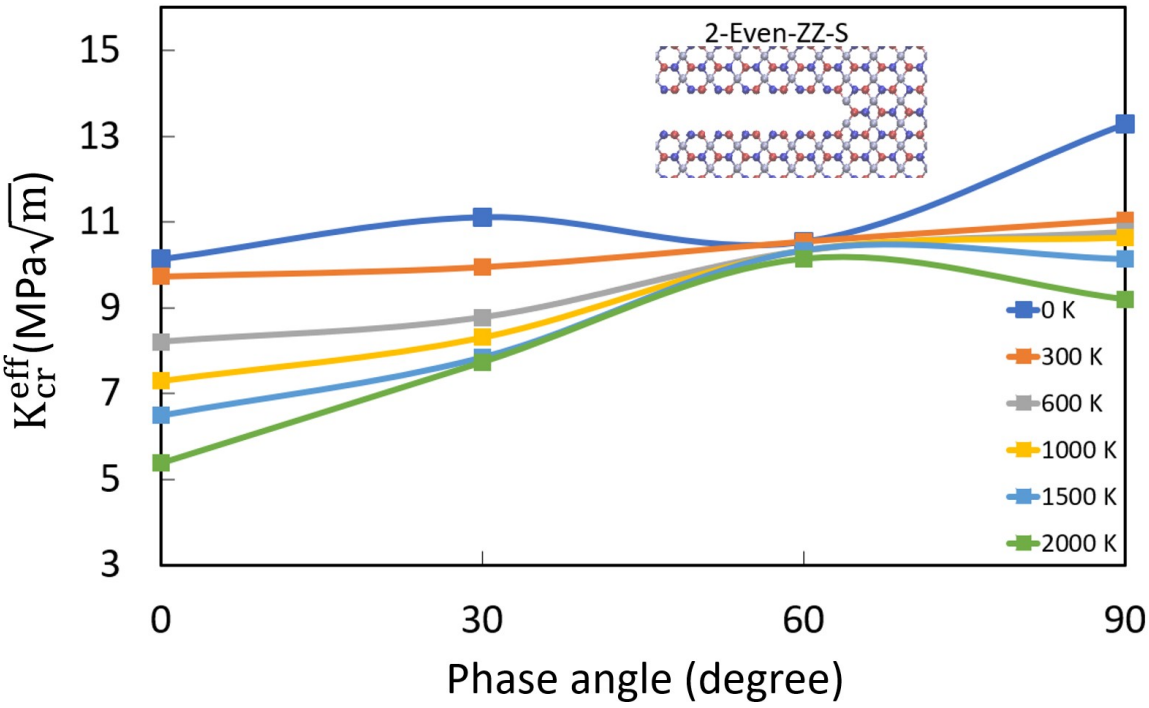

Figure 4.15: Temperature effect on critical stress intensity factor for TG-2-even.

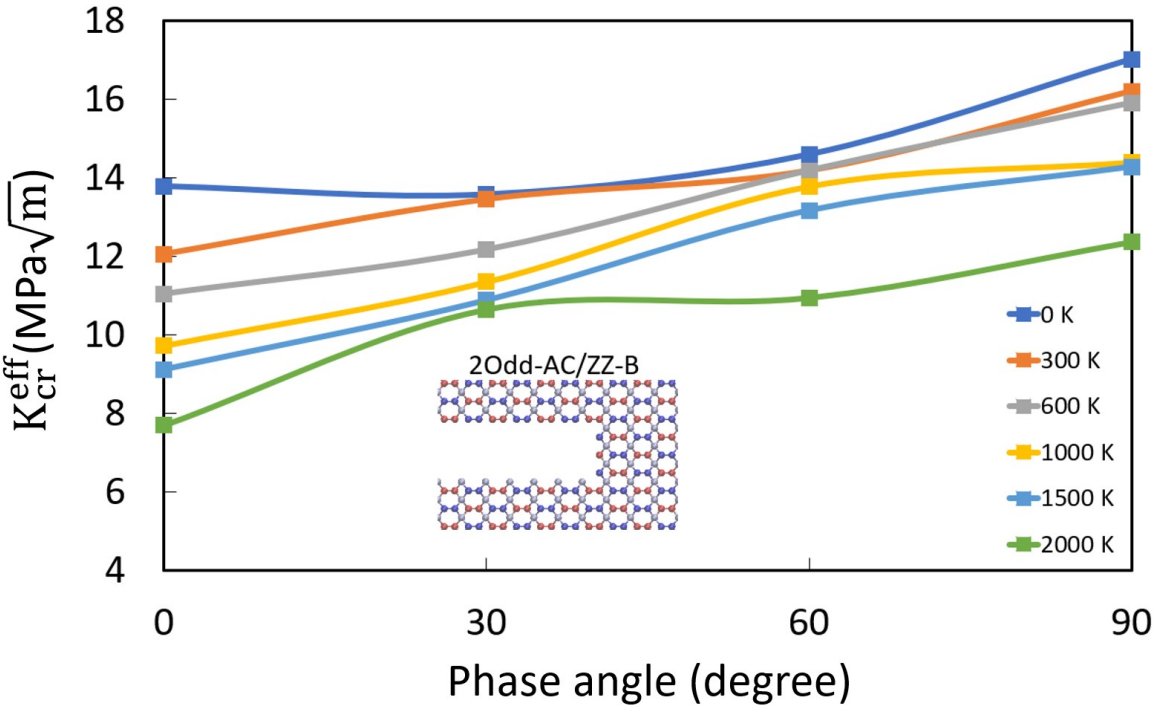

Figure 4.16: Temperature effect on critical stress intensity factor for TG-2-odd.

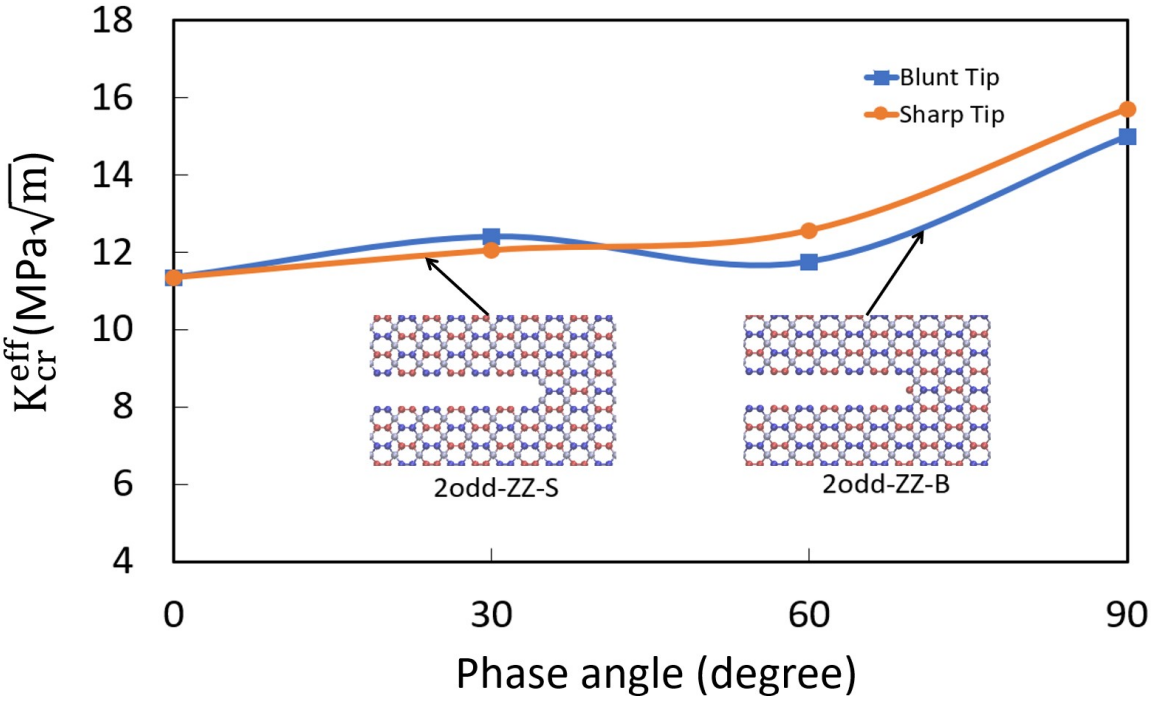

Figure 4.17: Crack tip configuration effect on critical stress intensity factor.

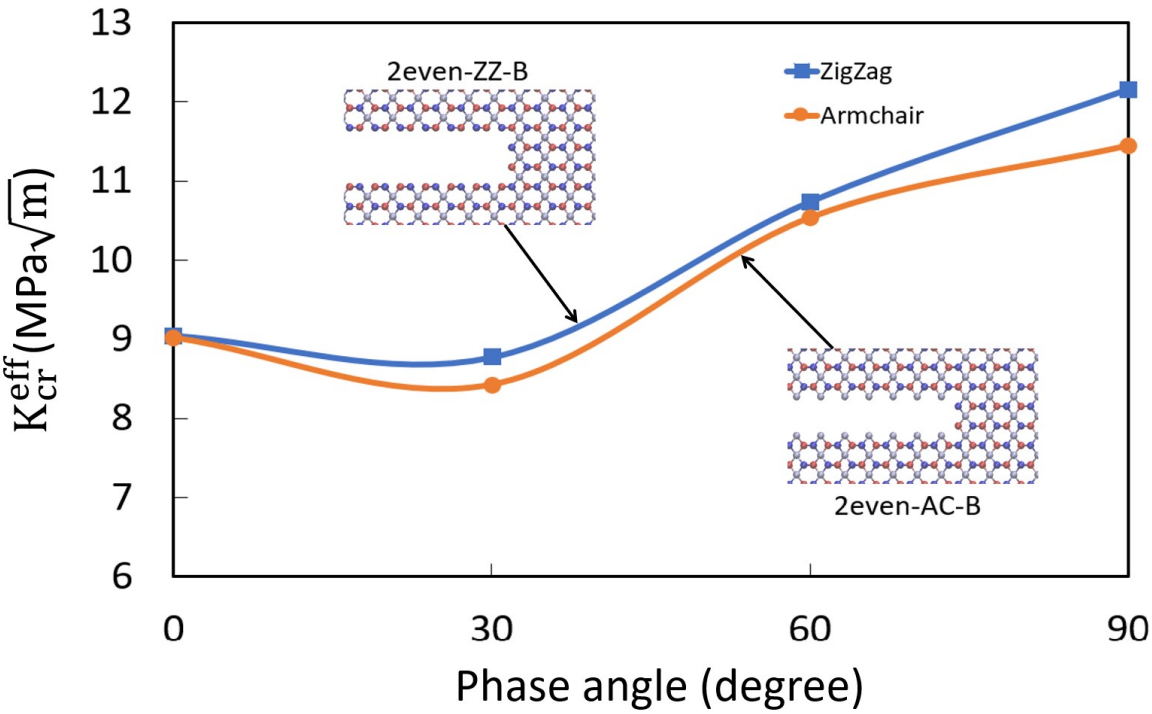

Figure 4.18: Crack edge chirality effect on critical stress intensity factor.

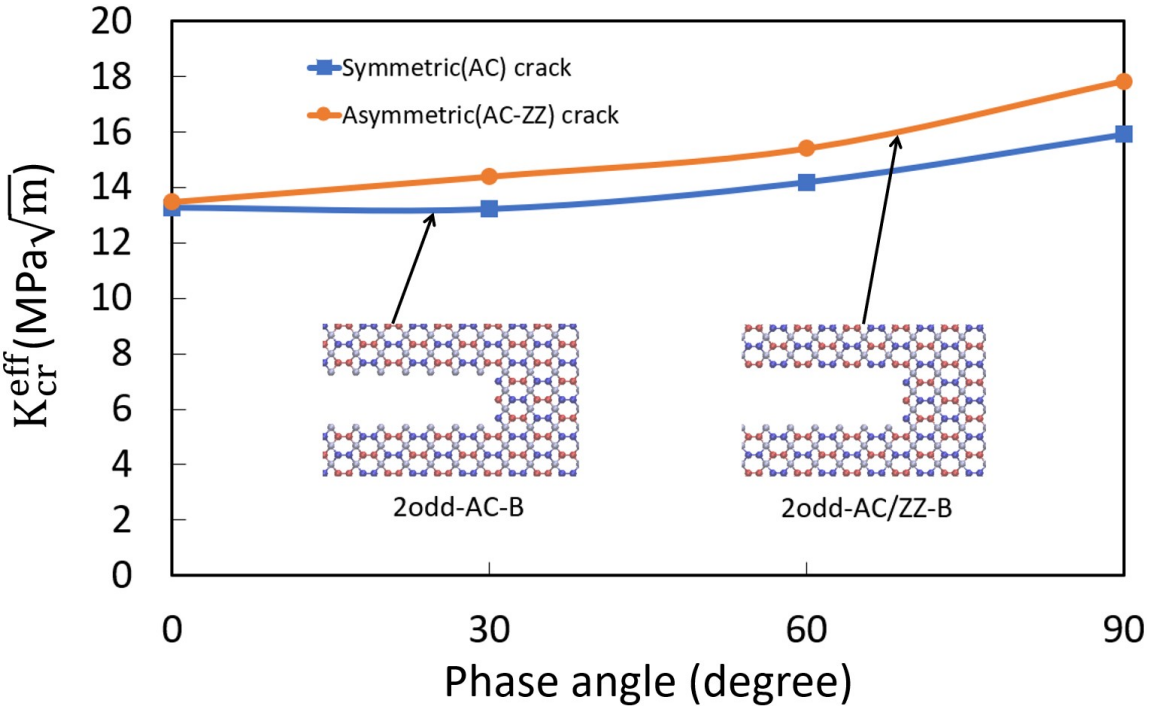

Figure 4.19: Crack symmetry/asymmetry effect on critical stress intensity factor for TG-2-odd.

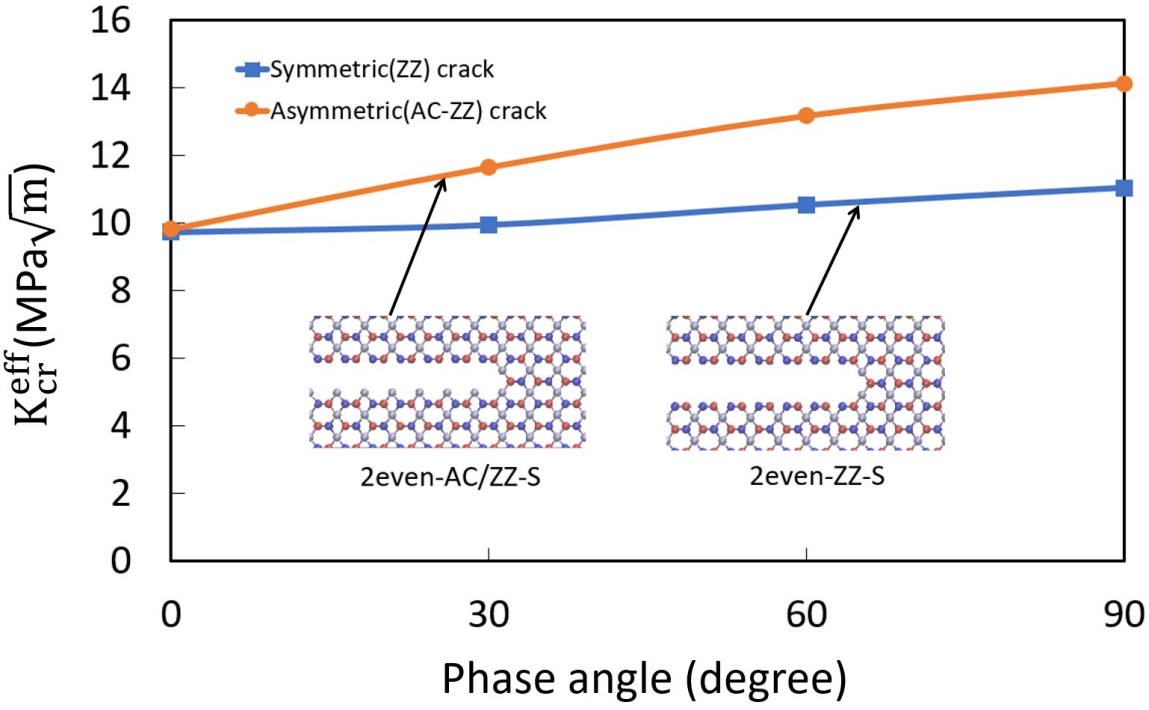

Figure 4.20: Crack symmetry/asymmetry effect on critical stress intensity factor for TG-2-even.

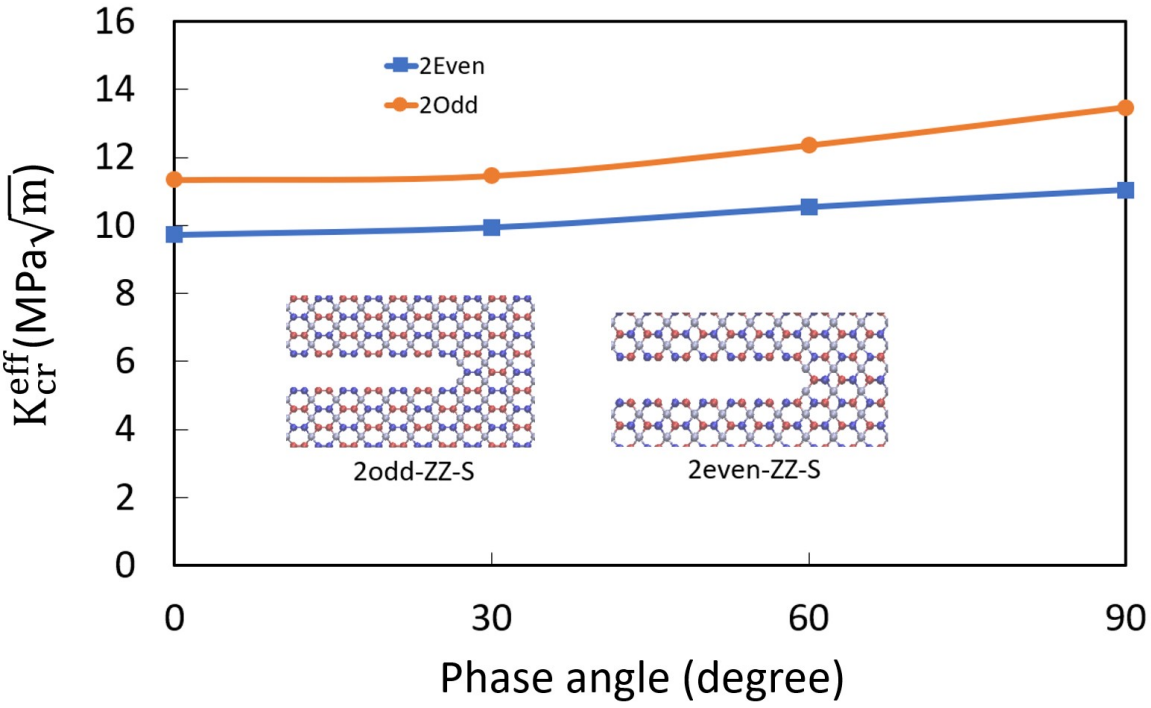

Figure 4.21: Comparison of TG-2-even and TG-2-odd in terms of critical stress intensity factor.

4.5 Conclusion

This project investigated the critical stress intensity factor and crack propagation paths in TG-2-even and TG-2-odd structures, considering various factors such as loading phase angle, temperature, crack edge chirality, and crack tip configuration. The results demonstrated that by increasing the loading phase angle, the critical stress intensity factor would increase as well. For loading phase angles greater than zero, cracks exhibit kinking as they grow, with minimum and maximum out-of-plane deformation corresponding to mode I and mode II loading, respectively. It is concluded that crack propagation under shearing mode (mode II) requires more energy compared to opening mode (mode I) due to the generation of out-of-plane deformation.

Furthermore, Increasing temperature led to a decrease in stress intensity factor for both 2-even and 2-odd structures. The study also found that zigzag cracks generally exhibit higher values of stress intensity factor compared to armchair cracks. Additionally, asymmetric cracks generally showed higher stress intensity factors. Additionally, the influence of the crack tip configuration depends on the loading phase angle. Overall, the mode I stress intensity factor is not affected by crack edge chirality, crack tip configuration, and crack symmetry. Lastly, the comparison between TG-2-even and TG-2-odd structures revealed that the 2-odd structure generally has a higher critical stress intensity factor.

REFERENCES

[1] Martin Pumera. Electrochemistry of graphene: new horizons for sensing and energy storage. *The Chemical Record*, 9(4):211–223, 2009.

[2] Mohan SR Elapolu, Alireza Tabarraei, Xiaonan Wang, and Douglas E Spearot. Fracture mechanics of multi-layer molybdenum disulfide. *Engineering Fracture Mechanics*, 212:1–12, 2019.

[3] Brett Leedahl, Zahra Abooalizadeh, Kyle LeBlanc, and Alexander Moewes. Tunability of room-temperature ferromagnetism in spintronic semiconductors through nonmagnetic atoms. *Physical Review B*, 96(4):045202, 2017.

[4] Alireza Tabarraei, Xiaonan Wang, and Dan Jia. Effects of hydrogen adsorption on the fracture properties of graphene. *Computational Materials Science*, 121:151–158, 2016.

[5] Alireza Tabarraei and Xiaonan Wang. Anomalous thermal conductivity of monolayer boron nitride. *Applied Physics Letters*, 108(18), 2016.

[6] Xiaonan Wang and Alireza Tabarraei. Phonon thermal conductivity of monolayer mos2. *Applied Physics Letters*, 108(19), 2016.

[7] Kaveh Safavigerdini, Koundinya Nouduri, Ramakrishna Surya, Andrew Reinhard, Zach Quinlan, Filiz Bunyak, Matthew R Maschmann, and Kannappan Palaniappan. Predicting mechanical properties of carbon nanotube CNT images using multi-layer synthetic finite element model simulations. *arXiv preprint arXiv:2307.07912*, 2023.

[8] Bart Partoens and FM Peeters. From graphene to graphite: Electronic structure around the K point. *Physical Review B*, 74(7):075404, 2006.

[9] Andre K Geim and Konstantin S Novoselov. The rise of graphene. *Nature materials*, 6(3):183–191, 2007.

[10] Qun Wei, Guang Yang, and Xihong Peng. Auxetic tetrahex carbon with ultrahigh strength and a direct band gap. *Physical Review Applied*, 13(3):034065, 2020.

[11] Mei Xu, Alireza Tabarraei, Jeffrey T Paci, Jay Oswald, and Ted Belytschko. A coupled quantum/continuum mechanics study of graphene fracture. *International journal of fracture*, 173(2):163–173, 2012.

[12] Bin Zhang, Lanjv Mei, and Haifeng Xiao. Nanofracture in graphene under complex mechanical stresses. *Applied Physics Letters*, 101(12):121915, 2012.

[13] Mohammed A Rafiee, Javad Rafiee, Iti Srivastava, Zhou Wang, Huaihe Song, Zhong-Zhen Yu, and Nikhil Koratkar. Fracture and fatigue in graphene nanocomposites. *small*, 6(2):179–183, 2010.

[14] Zahra Abooalizadeh, Leszek Josef Sudak, and Philip Egberts. Nanoscale spatial mapping of mechanical properties through dynamic atomic force microscopy. *Beilstein journal of nanotechnology*, 10(1):1332–1347, 2019.

[15] Zahra Abooalizadeh, Peng Gong, Leszek Sudak, and Philip Egberts. Layer dependent out-of-plane elastic modulus of graphene. *Applied Physics Letters*, 118(26), 2021.

[16] Wjefferson HS Brandão, Acrisio L Aguiar, Alexandre F Fonseca, DS Galvão, and JM De Sousa. Mechanical properties of tetragraphene single-layer: A molecular dynamics study. *Mechanics of Materials*, 176:104503, 2023.

[17] Fabrício Morais De Vasconcelos, Antônio Gomes Souza Filho, Vincent Meunier, and Eduardo Costa Girão. Electronic properties of tetragraphene nanoribbons. *Physical Review Materials*, 3(6):066002, 2019.

[18] Fabrício Morais de Vasconcelos, Antonio Gomes Souza Filho, Vincent Meunier, and Eduardo Costa Girão. Electronic and structural properties of tetragraphenes. *Carbon*, 167:403–413, 2020.

[19] Babu Ram and Hiroshi Mizuseki. Tetrahexcarbon: A two-dimensional allotrope of carbon. *Carbon*, 137:266–273, 2018.

[20] Mehmet Emin Kilic and Kwang-Ryeol Lee. Tuning the electronic, mechanical, thermal, and optical properties of tetrahexcarbon via hydrogenation. *Carbon*, 161:71–82, 2020.

[21] Mehmet Emin Kilic and Kwang-Ryeol Lee. First-principles study of fluorinated tetrahexcarbon: stable configurations, thermal, mechanical, and electronic properties. *The Journal of Physical Chemistry C*, 124(15):8225–8235, 2020.

[22] Steve Plimpton. Fast parallel algorithms for short-range molecular dynamics. *Journal of computational physics*, 117(1):1–19, 1995.

[23] Paul Erhart and Karsten Albe. Analytical potential for atomistic simulations of silicon, carbon, and silicon carbide. *Physical Review B*, 71(3):035211, 2005.

[24] Ted L Anderson. *Fracture mechanics: fundamentals and applications*. CRC press, 2017.

[25] Roberto Brighenti. Buckling of cracked thin-plates under tension or compression. *Thin-Walled Structures*, 43(2):209–224, 2005.